Structures 31 (2021) 740–760

Contents lists available at ScienceDirect

Structures

journal homepage: www.elsevier.com/locate/structures

Mechanics of damage in reinforced concrete member under post-blast fire scenario

Tathagata Roy, Vasant Matsagar [*,1]

Multi-Hazard Protective Structures (MHPS) Laboratory, Department of Civil Engineering, Indian Institute of Technology (IIT) Delhi, Hauz Khas, New Delhi - 110 016, India

ARTICLE INFO

Keywords:
Blast
Cascading
Damage
Finite element
Fire
Post-blast fire
RC wall panel

ABSTRACT

Recent terrorist activities in the form of blast and its cascading effects in the form of fire have had devastating impacts in structures, posing serious safety issues in structural members. In this context, a numerical study is conducted here to investigate the mechanics of damage in a reinforced concrete (RC) wall panel exposed to post-blast fire. The study involves developing a three-dimensional (3-D) nonlinear finite element (FE) model considering material nonlinearity as well as geometric nonlinearity. The developed FE model of the RC wall panel is first exposed to blast scenario, where the dynamic effect of blast loading is incorporated using strain-rate-dependent models of concrete and steel. The subsequent transient thermo-mechanical analysis, considering pre-damaging effects of the RC wall panel, is carried out by duly incorporating the temperature variation in thermal and mechanical properties of concrete and steel reinforcing bars. Responses are compared in terms of out-of-plane deflection, variation in stresses and strains at exposed and unexposed faces, damage pattern, and nodal temperatures of the wall panel. It is concluded that the responses obtained under the cascaded extreme loading scenario demonstrate significant damage caused to the RC wall panel as compared to the damage induced when it is exposed to either of the particular hazards. Moreover, fire resistance rating of the wall panel decreases considerably under the extreme cascading effects. Hence, current design standards may be required to incorporate the pre-damaging effects of cascading hazard to safeguard civil infrastructures from such extreme accidental/ manmade threats.

1. Introduction

Design of structure and infrastructure systems against extreme manmade/accidental threats, such as, post-blast fire has become an escalating concern as observed from the recent catastrophic devastations. The significance of such cascading threats was understood after the Oklahoma City bombing in 1995 and the World Trade Center (WTC) collapse in 2001, in which major structural systems experienced triggered effects of fire after explosion. The catastrophes had inflicted about 10,000 fatalities with more than US$ 10 billion in property and infrastructure damages, and about US$ 3 trillion in total costs [19,20,65]. Moreover, in India, recent Mumbai factory blast in 2016, caused by explosion of flammable gas, has shown that the structures have increased vulnerability under the cascaded shock and high temperature effects. In such attacking scenarios, the structural elements tend to lose the required load-carrying capacity upon exposure to blast or extreme impulse-type loading, which subsequently has the possibility to affect the structural fire behavior significantly [4,67,71,72]. In this regard, it is imperative that the most important structural members are properly designed against the actions of such cascading hazard scenarios. Hence, it becomes important to address the challenging effects of cascading hazards on structure and infrastructure systems to sustain local damage without global collapse [69]. Therefore, the prime objective of structural design should address such complex interaction effects to assess and enhance the structural resistance under the extreme threats of post-blast fire.

Reinforced concrete (RC) structures, as compared to steel structures, have higher fire resistance by virtue of its physical/ mechanical properties. Despite having relatively higher fire-resistant features, concrete is extremely sensitive to rate of loading and high temperature. Dynamic

* Corresponding author at: Multi-Hazard Protective Structures (MHPS) Laboratory, Department of Civil Engineering, Indian Institute of Technology (IIT) Delhi, Hauz Khas, New Delhi - 110 016, India.
E-mail addresses: tathagata.roy@civil.iitd.ac.in (T. Roy), matsagar@civil.iitd.ac.in (V. Matsagar).
[1] Dogra Chair Professor.

https://doi.org/10.1016/j.istruc.2021.02.005
Received 23 October 2020; Received in revised form 20 January 2021; Accepted 2 February 2021
Available online 27 February 2021

impulsive loading, such as blast, has high rate of loading, which induces relatively higher strain-rate in concrete. The dynamic inertia effect under the high strain-rate induced by blast loading changes the cracking pattern of concrete as compared to the static state [21], which induces damage with gradual reduction in strength and stiffness of concrete. Such damaging impact under the extreme blast loads often results in extensive compressive crushing and spalling of concrete, exposure of reinforcement bar, and failure of the structural elements due to shear/flexure cracks [18,49]. Now, with occurrence of fire after being inflicted with some degree of damage due to the blast event, the structural system experiences relatively more damage under the fire loading, as this phenomenon introduces more micro-structural changes in already pre-damaged concrete, leading to increased deformation under the cascaded fire scenario. The damage induced on the RC members under the blast loading alters the heat transfer mechanism and temperature distribution in structural member, which in turn deteriorates the already degraded load-bearing capacity of the structure [54]. In such critical scenario, transfer of heat is relatively faster to the core of the RC member through the induced cracks and spalling, thereby reducing the strength drastically at comparatively lesser temperatures. In this regard, understanding the fundamental behavior of a pre-damaged structure under fire becomes extremely important, as this phenomenon substantially alters the performance of structure [8]. Hence, the novel analysis and design strategy will serve the purpose of improving the integrity, stability, and survivability of concrete structures under the cascaded effects of post-blast fire. This is specifically important in petrochemical industries, design of protective structures in nuclear installments, and in the thermal power stations.

Early studies, however limited, were conducted to investigate structural response under blast loading and elevated temperature, independently [61]. Thereafter, ability of structures to sustain local damage without global collapse under the complex effects of cascading scenarios required urgent attention. Assessment of the complex cascading effects generally started progressing in last decade to quantify the damage induced in structures [63]. Gradually, research included the use of unique techniques, such as, fiber-element approach to assess the performance of structures exposed to combined effect of blast and fire [46]. The method accurately captured the detailed behavior of member and frame instability related to high strain-rate and temperature effects. The interaction effects were more notable in steel structures as compared to the reinforced concrete (RC) structures due to lower fire resistance. Thereafter, resilience of structural members constructed with innovative materials, as concrete-filled fiber reinforced polymer (FRP) used in tubular columns (CFFT) for bridge under extreme loadings such as blast and fire, was also assessed [24]. The study promoted the use of new light reinforced CFFT columns to enhance the multi-hazard resistance of the bridge piers. Kakogiannis et al. [36] investigated the blast-resisting capacity of RC hollow core slabs under fire following blast. On an interesting note, the fire load altered blast load responses and crack patterns with temperatures rising upto 450 °C. Recent studies include cascading effects of explosion and fire on underground structures [16,57]. Spalling of concrete occurred under the interaction effects of both explosion and increased temperature leading to a reduced thickness of the load bearing structure. Materials respond differently when exposed to blast loads, which requires transient dynamic nonlinear analysis for computing the response [50–52]. Few experimental studies were conducted to investigate the thermo-mechanical behavior of concrete under combined effects of high temperature and high strain-rate loading [14,70]. Constitutive models considering coupled effects of high temperature and high strain-rate for concrete were proposed. Recent practical applications included investigating dynamic responses of reactive powder concrete filled steel tubular (RPC-FST) columns under post-fire blast loading [68]. The RPC-FST columns possessed excellent blast-resistant capabilities after being exposed to fire. Jin et al. [35] analyzed steel fiber-reinforced concrete (SFRC) beams under combined effects of blast-induced impact loading and fire. They concluded that at relative lower impact energy, though weakened by pre-impact, the SFRC beam showed good fire resistance. Under the multi-hazard scenario of two distinct cascaded loading conditions emanating from the blast and fire, the transient thermo-mechanical analysis by duly considering material and geometric nonlinearities is required to evaluate the structural response [53]. Of-late, research on the RC structures, considering the abovementioned practical applications to structural design under exceptional load cases, such as sudden heating or cooling, or high-dynamic strength of specimens are being reported [10]. More recently, Jin et al. [34] addressed that fire duration plays a significant role in structural failure when the pre-damaging scenario is considered. In this context, research involved till the date is limited, which accounts for possible pre-damaging effects with a viewpoint to understand the behavior of structures through the mechanics involved under the effect of cascading post-blast fire. Though, Roy and Matsagar [59] have studied vulnerability of fire-exposed RC panels under transverse out-of-plane and compressive in-plane loads, they did not consider strain-rate-dependent pre-loading emanating from the blast load but considered imposed gravity loads. Therefore, it becomes essential to investigate the behavior of structure under cascaded fire loading after considering the induced dynamic strain-rate effects due to extreme blast loading. Developing such an analysis framework will provide a reliable approach for protection of structures against more severe cascaded fire to guarantee stability of structure and obtain adequate time to control the fire spread and safely evacuate the inhabitants in the structure.

An assessment of a three dimensional (3-D) reinforced concrete (RC) structural member is conducted in the present work, considering pre-damaged effect due to a blast event followed by cascading fire event. Deterministic cascading loading scenario is considered in the post-blast fire loading in which the blast loading is followed by the thermal loads applied because of the fire hazard. Responses, such as, displacement, membrane stresses and strains, and damage quantities are investigated for the individual blast and fire loading cases, and assessment is made with the cascaded post-blast fire scenario. In the context of the abovementioned scope, the specific objectives defined are: (i) to understand the behavior and mechanism of deformation of the RC structural member under the effect of post-blast fire, (ii) to compare the responses and conduct parametric studies for different member sizes to propose design requirements for the range of blast loadings adopted, and (iii) to compare fire resistance rating of the RC members under normal and cascaded post-blast fire scenarios.

2. Plasticity-based modeling of concrete and steel

The behavior of RC structural member is mainly dependent on behavior of concrete and steel, which conversely is reliant on available plasticity models along with their respective constitutive laws. Concrete exhibits extreme nonlinearity under the effect of dynamic loads as compared to static and quasi-static loads due to the development of micro-cracking. Failure in concrete under compression is relatively more complex, which involves volumetric expansion, strain localization, crushing, and ductile hardening followed by softening and reduction in the unloading stiffness for the stress–strain behavior [2]. On the other hand, failure in concrete is localized in narrow band under tension. However, in mixed stress conditions, the failure generally depends on the ratio between the principal stresses, i.e., in tension–compression state, and the failure occurs under the compression induced in the material between the cracks. In this regard, to capture the nonlinearity of concrete, coupling between damage and plasticity models is crucial. Concrete damaged plasticity (CDP) model is one such plasticity model that captures nonlinearity in concrete, as the given multiaxial model considers simultaneous combination of isotropic damaged elasticity and non-associated multi-hardening plasticity. The CDP model in ABAQUS® is a combined model of Lubliner et al. [48], and the modifications proposed by Lee and Fenves [43] to account for different evolution of

strength under tension and compression. In other words, this CDP model is suited well to reproduce failure modes based on compression crushing and tensile cracking [52].

A typical uniaxial stress–strain plot under compression consists of loading and unloading branches of plasticity model, damage model, and combination of damage-plasticity model. The CDP model utilizes the uniaxial compressive and tensile stress–strain characteristics of concrete through damaged plasticity, in which the damage-plasticity behavior for compression and tension under uniaxial loading is given as,

$$\sigma_c = (1 - d_c)E_0\left(\varepsilon_c - \varepsilon_c^{pl}\right) \tag{1}$$

$$\sigma_t = (1 - d_t)E_0\left(\varepsilon_t - \varepsilon_t^{pl}\right) \tag{2}$$

where, E_0 is the initial elastic modulus, σ_c and ε_c^{pl}, and σ_t and ε_t^{pl} denote the stress and plastic strain under uniaxial compression c and tension t, respectively, whereas ε_c and ε_t respectively represent strains for given σ_c and σ_t. For cyclic loading–unloading state, the degradation in the elastic modulus for the CDP model is given by the reduced tangent modulus, $E = (1\text{-}d)E_0$; where, the scalar damage variable, d represents scalar damage measure ranging from 0 to 1, is a function of stress state, with the slope of unloading/reloading branch as $(1 - d)E_0$. The user-provided uniaxial stress versus (total) inelastic strain data is converted into stress versus plastic-strain curves using Eqs. (1) and (2). Further, the compression and tension damage variables, d_c and d_t, respectively, maybe expressed as,

$$1 - d = (1 - s_t d_c)(1 - s_c d_t) \tag{3}$$

where, s_t and s_c are dimensionless coefficients considering stress state and stiffness recovery effects (directly related to the elastic modulus), which are given by the following relations,

$$s_c = 1 - h_c[1 - r^*(\sigma_{11})] \tag{4}$$

$$s_t = 1 - h_t r^*(\sigma_{11}) \tag{5}$$

where, h_c indicates cracks re-closing after tension–compression reversal, h_t indicates recovery of concrete in crushing after compression-tension reversal. For example, $h_c = 0.8$ and $h_t = 0.15$ means that 80% of the cracks close when subjected to tension–compression reversal and the crushed concrete experience 15% of its recovery. In this regard, these dimensionless parameters, s_c and s_t range from 0 to 1. Moreover, σ_{11} is the first principal uniaxial stress (negative for compression and positive for tension), r^* is a stress state parameter given as $r^*(\sigma_{11}) = 0$ for compression and 1 for tension. Simultaneously, for multi-axial state of stress–strain, the relationship may be given as,

$$\sigma = (1 - d)D_0^{el} : \left(\varepsilon - \varepsilon^{pl}\right) \tag{6}$$

where, σ is Cauchy stress tensor, ε is strain tensor, D_0^{el} is initial or elastic stiffness tensor. The yield surface of the CDP model, based on loading F that accounts for evolution of tensile and compressive strengths, is given by [43,44,48],

$$F = \frac{1}{1 - \overline{\alpha}}\left[q - 3\overline{\alpha}p + \overline{\beta}\left(\varepsilon^{pl}\right)\langle\sigma_{max}\rangle - \overline{\gamma}\langle -\sigma_{max}\rangle\right] - \sigma_c\left(\varepsilon^{pl}\right) = 0 \tag{7}$$

$$\overline{\alpha} = \frac{(f_{b0}/f_{c0}) - 1}{2(f_{b0}/f_{c0}) - 1}; \quad 0 \le \overline{\alpha} \le 0.5 \tag{8}$$

$$\overline{\beta} = \frac{\overline{\sigma}_c}{\overline{\sigma}_t}(1 - \overline{\alpha}) - (1 + \overline{\alpha}) \tag{9}$$

$$\overline{\gamma} = \frac{3(1 - K_c)}{2K_c - 1} \tag{10}$$

where, $\overline{\alpha}$, $\overline{\beta}$, and $\overline{\gamma}$ are dimensionless constants, p represents hydrostatic pressure stress, q is von Mises equivalent stress obtained by stress divided by $1 - d$, f_{b0}, and f_{c0} represent biaxial and uniaxial compressive yield strengths, respectively, α ranges between 0 and 0.5 for $f_{b0} = f_{c0}$ and $f_{b0} \gg f_{c0}$, respectively, $\langle\bullet\rangle$ represents Macaulay bracket indicating the quantities within the bracket take either zero or positive values, σ_{max} represents the maximum principal effective stress, $\overline{\sigma}_c = \sigma_c/(1 - d)$ and $\overline{\sigma}_t = \sigma_t/(1 - d)$ represent effective compressive and tensile cohesion stress, respectively, and K_c is the ratio of second deviatoric stress invariant on tensile to that of the compressive meridians, which ranges from 0.5 (Rankine yield surface) to 1 (von Mises yield surface). For the current study, K_c is obtained using Mohr-Coulomb yield surface, which is given as,

$$H(\overline{\rho}, \overline{\xi}, \overline{\theta}, \overline{\varphi}, \overline{c}) = \sqrt{2}\overline{\xi}\sin\overline{\varphi} + \sqrt{3}\overline{\rho}\cos\overline{\varphi} - \overline{\rho}\sin\overline{\theta}\sin\overline{\varphi} - \sqrt{6}\overline{c}\cos\overline{\varphi} = 0 \tag{11}$$

where, $\overline{\rho} = \sqrt{(2\,J_2)}$ represents octahedral radius, $\overline{\xi} = I_1/\sqrt{3}$ is the distance from stress space to stress plane, $\overline{\theta}$ represents Lode similarity angle, $\sin\overline{\theta} = 3\sqrt{3}J_3/(2\,J_2^{3/2})$, $\overline{\varphi}$ and $\overline{c}$ represent friction angle and cohesion, respectively, I_1 represents 1st invariant of stress tensor, and J_2 and J_3 are 2nd and 3rd invariants of deviatoric stress tensors. Now, for $\overline{\xi} = 0$ and $\overline{\theta} = \pm\pi/6$, the values for deviatoric stress invariant on tensile and compressive meridians are given as,

$$\overline{\rho}_{c0} = \frac{2\sqrt{6}\overline{c}\cos\overline{\varphi}}{3 - \sin\overline{\varphi}}; \ \overline{\rho}_{t0} = \frac{2\sqrt{6}\overline{c}\cos\overline{\varphi}}{3 + \sin\overline{\varphi}} \tag{12}$$

Hence,

Table 1
Parameters used for the concrete damaged plasticity (CDP) model.

Dilation angle (ψ)	Eccentricity (e)	f_{b0}/f_{co}	K_c
36.31	0.1	1.16	0.667

Table 2a
Damage parameters (d_c) used for the concrete damaged plasticity (CDP) model under compression due to high strain rate and thermal loadings.

Loading	Compression damage, d_c	Plastic strain (ε_{pl})	Temperature (°C)
Blast	0	0	–
	0.2162	0.002575	–
	0.3515	0.003789	–
	0.3749	0.003955	–
	0.4722	0.00454	–
	0.6766	0.00651	–
	0.8533	0.0085	–
Fire	0	0	20
	0.00393	0.6355	20
	0.00609	0.8126	20
	0.9319	0.0098	20
	0.9444	0.0106	20
	0.9673	0.0132	20
	0	0	100
	0.6664	0.005845	100
	0.8233	0.009732	100
	0.8649	0.011549	100
	0	0	200
	0.3900	0.005791	200
	0.6869	0.008914	200
	0.8300	0.014745	200
	0	0	300
	0.5693	0.007113	300
	0.6771	0.010318	300
	0.7532	0.013418	300
	0	0	400
	0.6486	0.010761	400
	0.7241	0.014028	400
	0.0000	0.01122	500
	0.6271	0.01364	500
	0.7021	0.01465	500

Table 2b
Damage parameters (d_t) used for the concrete damaged plasticity (CDP) model under tension due to high strain rate and thermal loadings.

Loading	Tension damage, d_t	Plastic strain (ε_{pl})	Temperature (°C)
Blast	0	0	–
	0.0155	0.000035	–
	0.1950	0.000482	–
	0.3594	0.000990	–
	0.6746	0.002495	–
	0.8945	0.004997	–
	0.9889	0.009998	–
Fire	0	0	20
	0.8654	0.109999	20
	0	0	100
	0.8529	0.109999	100
	0	0	200
	0.8197	0.109999	200
	0	0	300
	0.7256	0.109999	300
	0	0	400
	0.6984	0.109999	400
	0	0	500
	0.6318	0.109998	500
	0	0	700
	0.5918	0.109997	700
	0	0	800
	0.5163	0.109996	800

$$K_c = \frac{\overline{\rho}_{c0}}{\overline{\rho}_{t0}} = \frac{3 - \sin\overline{\varphi}}{3 + \sin\overline{\varphi}} \tag{13}$$

The CDP model follows non-associated flow with potential plastic surface, G, which uses Drucker-Prager hyperbolic function, given as,

$$G = \sqrt{(\in \sigma_{t0} tan\psi)^2 + q^2} - ptan\psi \tag{14}$$

where, $\in$ is the eccentricity parameter of plastic potential surface, σ_{t0} is the uniaxial tensile stress at failure, ψ represents the dilation angle measured in the mean stress – deviatoric stress plane, that defines amount of plastic volumetric strain induced in plastic shear.

To summarize, in the CDP model, eight governing parameters define the constitutive law/relation as follows: (i) dilation angle (ψ) defines amount of plastic volumetric strain induced in plastic shear, (ii) flow potential eccentricity ($\in$) in the stress–strain relation shows the rate at which the function approaches asymptote in the hyperbolic surface of plastic potential in meridional plane, (iii) K_c parameter controls the shape of yield surface, (iv) the ratio, f_{b0}/f_{c0}, typically exhibits multi-axial to uniaxial material strengths, (v) and (vi) correspond to two damage parameters (d_c and d_t) to simulate the damage occurring due to degradation in strength and stiffness under post-blast scenario, and (vii) and (viii) refer to two recovery parameters, i.e., h_c and h_t for compression and tension which are typically defined when reversal of stresses is possible and material does show peculiar behavior in its stiffness changes when tensile and compressive stresses are reversed. The first four parameters are plasticity parameters for concrete, which are provided in Table 1. Table 2(a) and 2(b) correspond to the damage parameters (d_c and d_t) used for the CDP model under compression and tension, respectively due to strain-rate and thermal loadings. Finally, two recovery parameters, i.e., h_c and h_t for compression and tension are respectively chosen as 0.75 and 0.15. The solution procedure for the CDP model in nonlinear domain in ABAQUS®, in general, utilizes backward-Euler method and spectral return-mapping, as proposed by Lee and Fenves [45]. The 3-D and plane stress formulations of the return-mapping algorithm for the CDP model are derived using the spectral decomposition form of the stress matrix. The main advantage herein is that the spectral return-mapping algorithm efficiently solves constitutive equations in the CDP model that contain many principal stresses and the eigenvalues of incremental plastic strains.

On the other hand, classical metal plasticity model is used for reinforcing bar as this model is effective in depicting the behavior of metals under impact and cyclic loadings. The classical metal plasticity model uses von Mises yield surface with associated plastic flow, which allow to undergo isotropic hardening of the material. This model is very much effective to investigate the strain-rate dependence of the material. The constitutive model of plastic material includes a yield condition, a flow rule, and a hardening law. The post-yielding behavior of steel rebar is incorporated by classical metal plasticity model using von Mises yield criterion with associated plastic flow and isotropic hardening. The yield surface is defined using von Mises yield criterion, which is given by the function,

$$f(\widehat{\sigma} - \widehat{\alpha}) = \widehat{\sigma}^0 \tag{15}$$

$$f(\widehat{\sigma} - \widehat{\alpha}) = \sqrt{\frac{3}{2}(S - \widehat{\alpha}^{dev}) : (S - \widehat{\alpha}^{dev})} \tag{16}$$

where, $f(\widehat{\sigma} - \widehat{\alpha})$ represents the equivalent Mises stress with respect to the backstress $\widehat{\alpha}$, and $\widehat{\sigma}^0$ is the size of the yield surface, $\widehat{\alpha}^{dev}$ represents the deviatoric part of the backstress, and S is the deviatoric stress tensor. Moreover, the flow rule is given by,

$$\dot{e}^{pl} = \partial f(\frac{\widehat{\sigma} - \widehat{\alpha})}{\partial\overline{\sigma}}\dot{\overline{e}}^{pl} \tag{17}$$

where, $\dot{e}^{pl}$ is the plastic flow rate, and $\overline{e}^{pl}$ represents the equivalent plastic strain-rate, given by,

$$\dot{\overline{e}}^{pl} = \sqrt{\frac{2}{3}\dot{e}^{pl} : \dot{e}^{pl}} \tag{18}$$

Since the material exhibits rate dependence behavior, overstress power law is used to define the rate dependence, which is defined by,

$$\dot{\overline{e}}^{pl} = D\left(\overline{\sigma}/\sigma^0 - 1\right)^n \tag{19}$$

where, D and n are user-defined material parameters defining the failure, σ^0 and $\overline{\sigma}$ represent static yield stress and yield stress at non-zero plastic strain, respectively. Hence, the behavior of reinforcing steel embedded in concrete is captured from the plastic values of the stress–strain curve and the rate-dependent parameters (D and n) that defines the failure of the material. For the present scenario, D and n are respectively assumed as 20 and 5 to simulate the damage in the steel reinforcing bar.

3. Material model

It is important to understand the behavior of the RC material through the available constitutive relationships in order to assess the accuracy of the responses. The RC material is rather complicated in nature, which warrants reliable model to inevitably capture both elastic and plastic behaviors in compression and tension. Hence, appropriate material models are required to be chosen carefully for capturing the nonlinearity of the RC materials under high strain-rate and thermo-mechanical effects.

3.1. Material model for blast analysis

The behavior of concrete under high strain-rate (i.e., dynamic) loading is quite different as compared to that under quasi-static loading as the combined phenomena is complex due to the combination of brittle nature and hydrostatic properties of concrete [47]. Likewise, the reinforcing steel bars exhibit a varying strain-rate effect under different loading rates mainly due to the type of materials used in various steel bar grades and evolution of dynamic dislocations, which affect the microscopic scale to a larger extent. The dynamic behavior of concrete and steel under high strain-rate loading is characterized by dynamic increase factor (DIF). The dynamic strength of these materials significantly

Table 3
Dynamic increase factors (DIFs) used for concrete and steel.

	Strain rates	DIFs
Concrete compression	10	1.02
	100	1.43
	250	1.89
	500	2.32
	1000	2.74
Concrete tension	10	3.56
	100	7.00
	250	8.77
	500	10.27
	1000	11.90
Steel tension	10	1.18
	100	1.21
	250	1.22
	500	1.23
	1000	1.24

increases with increasing strain-rate; hence, it is important to understand the physical mechanisms relating to the dynamic behavior of concrete and steel under different loading rates.

3.1.1. Strain-rate properties for blast analysis

The dynamic behavior of concrete under compression expressed in terms of the DIF for strain-rate, $\dot{\varepsilon}$ is described by the equation as follows [3],

$$\mathrm{DIF}^{c} = (3.54\dot{\varepsilon} + 430.6)/(\dot{\varepsilon} + 447.3) \tag{20}$$

The model can predict the DIF of concrete for strain-rate ranging from 10 to 1000 s^{-1}. Similarly, the DIF of concrete in tension for strain-rate can be given by the following equation [73],

$$\mathrm{DIF}^{t} = 0.7325(log\dot{\varepsilon})^2 + 1.235(log\dot{\varepsilon}) + 1.6 \tag{21}$$

where, superscripts *c* and *t* indicate the DIFs of concrete under uniaxial compression and tension for strain-rate, $\dot{\varepsilon}$.

The modulus of elasticity of concrete is similarly affected by the strain-rate induced due to dynamic loading. The increase in elastic modulus due to dynamic loading can be better described from the decrease in the internal micro-cracking at a given level of stress for increasing strain-rate. The strain-rate dependence model for the modulus of elasticity in terms of the DIF is obtained from the CEB-FIP Model Code 1990 (1993), which is given as,

$$\mathrm{DIF}^{E} = (\dot{\varepsilon}/\dot{\varepsilon}_0)^{0.026} \tag{22}$$

where, $\dot{\varepsilon}_0 = 3 \times 10^{-5}\ s^{-1}$ at quasi-static condition.

On the other hand, the reinforcing steel is similarly sensitive to strain-rate, which is observed significantly in yield stress, ultimate stress, and ultimate strain of the stress–strain curve [64]. In case of reinforcing steel, following expressions of the DIF for yield and ultimate stresses are used for the simulation, which are given as under [6],

$$\mathrm{DIF}^{y} = 1 + \frac{6}{f_y}\ln\frac{\dot{\varepsilon}}{\dot{\varepsilon}_0} \tag{23}$$

$$\mathrm{DIF}^{u} = 1 + \frac{7}{f_u}\ln\frac{\dot{\varepsilon}}{\dot{\varepsilon}_0} \tag{24}$$

where, DIF^{y} is the DIF for yield stress, f_y, DIF^{u} is the DIF for ultimate stress, f_u, and $\dot{\varepsilon}_0 = 5 \times 10^{-5}\ s^{-1}$ represents strain-rate at quasi-static condition. Finally, the DIFs for concrete in compression and tension, and steel are provided in Table 3.

3.1.2. Mechanical properties for blast analysis

The deformation of RC structures exposed to extreme blast loading is directly dependent on mechanical properties of concrete and steel. The stress–strain relationship of concrete under dynamic condition is approximated by the following functions given as under [17],

$$\sigma_c = -\frac{\frac{E_{ci}}{E_{c1}}\frac{\varepsilon_c}{\varepsilon_{c1}} - \left(\frac{\varepsilon_c}{\varepsilon_{c1}}\right)^2}{1 + \left(\frac{E_{ci}}{E_{c1}} - 2\right)\frac{\varepsilon_c}{\varepsilon_{c1}}} f_{cm}\ ;\ \varepsilon_c < \varepsilon_{c,lim} \tag{25}$$

$$\sigma_c = -\left[\left\{\left(\frac{\varepsilon_{c1}}{\varepsilon_{c,lim}}\xi - 2\left(\frac{\varepsilon_{c1}}{\varepsilon_{c,lim}}\right)^2\right)\right\}\left(\frac{\varepsilon_c}{\varepsilon_{c1}}\right)^2 + \left\{4\left(\frac{\varepsilon_{c1}}{\varepsilon_{c,lim}}\right) - \xi\right\}\right]^{-1} f_{cm}\ ;\ \varepsilon_c > \varepsilon_{c,lim} \tag{26}$$

$$\xi = \frac{4\left[\left(\frac{\varepsilon_{c,lim}}{\varepsilon_{c1}}\right)^2\left(\frac{E_{ci}}{E_{c1}} - 2\right) + 2\frac{\varepsilon_{c,lim}}{\varepsilon_{c1}} - \frac{E_{ci}}{E_{c1}}\right]}{\left[\frac{\varepsilon_{c,lim}}{\varepsilon_{c1}}\left(\frac{E_{ci}}{E_{c1}} - 2\right) + 1\right]^2} \tag{27}$$

where, σ_c is dynamic compressive stress of concrete (MPa) at strain ε_c, E_{ci} is tangent modulus of concrete in MPa, $\varepsilon_{c1} = 0.0022$ is the strain at maximum compressive stress of concrete, $E_{c1} = f_{cm}/\varepsilon_{c1}$ is the secant modulus at maximum dynamic compressive stress of concrete, f_{cm}, and $\varepsilon_{c,lim}$ is the limiting strain value after which the descending branch of the stress–strain curve originates. For given strain-rate, the dynamic strength can be calculated as $f_{cm} = \mathrm{DIF}^{*} \times f_{cms}$. The modulus of elasticity, E_{ci} can be estimated from the specified characteristic strength, f_{cms} given as under [56],

$$E_{ci} = (k_1 k_2)3.35 \times 10^4 (W_t/2400)^2 (f_{cms}/60)^{1/3} \tag{28}$$

where, k_1 is the correction factor for coarse aggregates, k_2 is the correction factor for mineral admixtures used in concrete, and W_t is the observed unit weight of concrete in kg/m^3. Finally, the effect of strain-rate on the elastic modulus is estimated, as given below,

$$E_{cid} = E_{ci} \times \mathrm{DIF}^{E} \tag{29}$$

where, E_{cid} is the modulus of elasticity at high strain-rate, and $\dot{\varepsilon}_0 = 3 \times 10^{-5}\ s^{-1}$ at the quasi-static condition.

The tensile strength of concrete under uniaxial loading is determined by the following expression,

$$f_{ctms} = 0.30 f_{cms}^{\ 2/3} \tag{30}$$

where, f_{ctms} is the tensile strength of concrete under quasi-static condition. For given strain-rate, the dynamic tensile strength can be calculated as $f_{ctmd} = \mathrm{DIF}^{*} \times f_{ctms}$. The constitutive relation defining the concrete under tension is given by the following equation,

$$\sigma_t = E_{cid}\varepsilon_t \quad ; \quad \varepsilon_t \le \varepsilon_{cr} \tag{31a}$$

$$\sigma_t = f_{ctmd}\left(\frac{\varepsilon_{cr}}{\varepsilon_t}\right)^n \quad ; \quad \varepsilon_t > \varepsilon_{cr} \tag{31b}$$

where, ε_{cr} is the strain at cracking of the concrete, and *n* is the post-peak rate of weakening.

The constitutive relation of the reinforcing steel under quasi-static state is adopted from the literature published by Silva and Lu [62]. Thereafter, the dynamic strengths of steel rebar are calculated by using the DIFs obtained from Eqs. (23) and (24).

3.2. Material model for thermal analysis

In order to predict the behavior of the fire-exposed RC wall panel after being subjected to the blast loading, the material properties at elevated temperatures after being exposed to blast scenario (pre-damaged condition) must be explicitly known to accurately determine

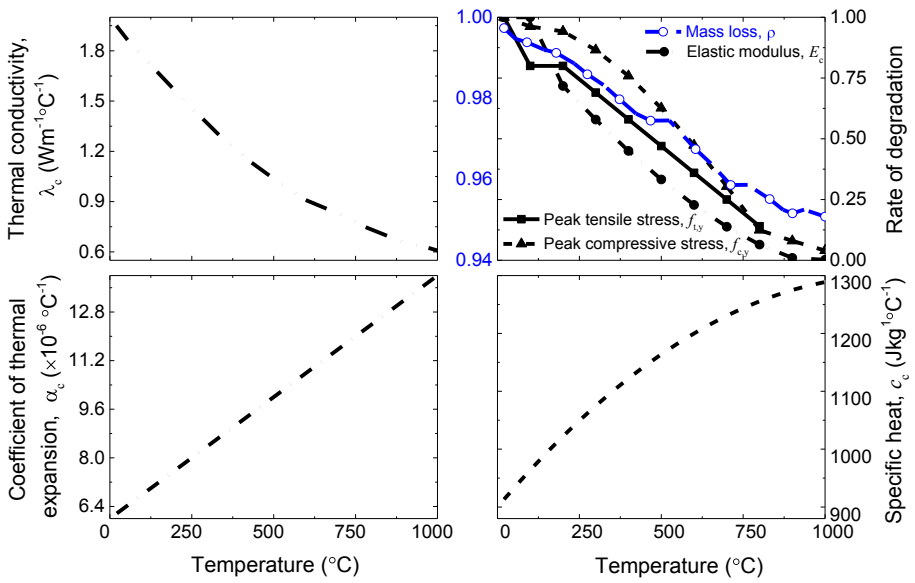

Fig. 1. Thermo-mechanical properties for concrete at elevated temperatures.

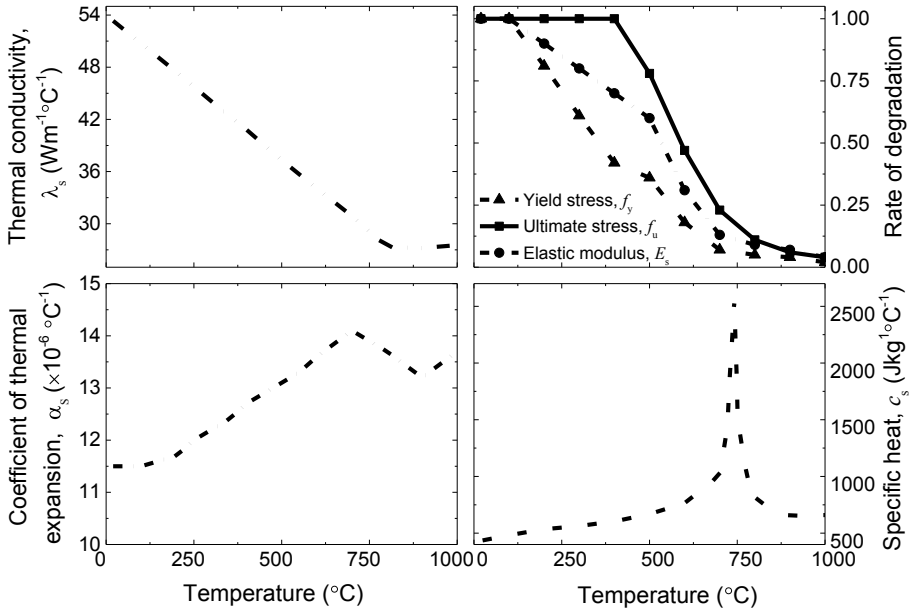

Fig. 2. Thermo-mechanical properties for steel at elevated temperatures.

the behavior of the structural members. However, current literature lacks information on the material properties at elevated temperature after subjecting to a certain damage level; hence, independent material models available for strain-rate and elevated temperature under quasi-static condition are used for the current analysis.

3.2.1. *Thermal properties for thermo-mechanical analysis*

The properties influencing the rise in temperature and its distribution in the concrete section and reinforcing bars are mass loss (ρ_c), thermal conductivity (k_c), coefficient of thermal expansion (α_c), and specific heat capacity (c_c) [9,40]. The mass loss, in terms of density, and thermal conductivity for normal strength concrete with siliceous aggregates are obtained from the widely accepted model of [23]. The mass loss is minimal for concrete with siliceous aggregate up to 1000 °C. Upper bound values of thermal conductivity are adopted for all types of aggregates, which are provided in widely accepted [23]. The coefficient of thermal expansion and specific heat capacity at temperature, T are expressed by the following equations [60,71],

$$\alpha_c = (0.008T + 6) \times 10^{-6} \tag{32}$$

$$c_c = -4\left(\frac{T}{120}\right)^2 + 80\left(\frac{T}{120}\right) + 900 \tag{33}$$

More importantly, the above-mentioned models overcome the abrupt increase in specific heat at temperature between 700 °C and 800 °C provided in the EC2 Part-1-2 [23]. The thermal conductivity, coefficient of thermal expansion, and specific heat capacity of the steel reinforcing bars at elevated temperature are based on the widely accepted models provided in the EC2 Part-1-2 [25]. The thermal properties for heat transfer analysis in concrete and steel are presented in Figs. 1 and 2.

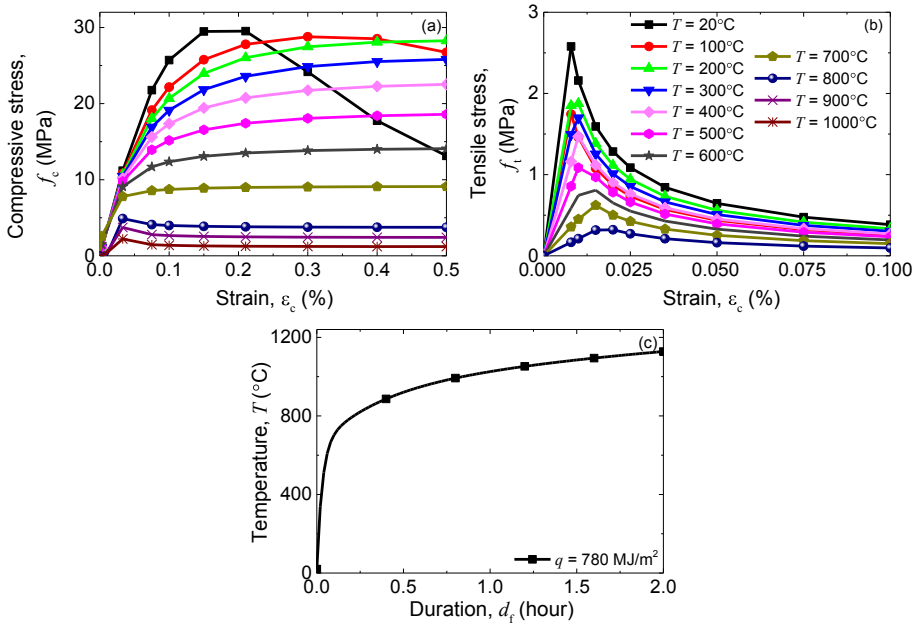

Fig. 3. Stress–strain relationship for concrete under (a) compression and (b) tension, and parametric fire curve for fuel load density, $q = 780$ MJ/m^2.

3.2.2. *Mechanical properties for thermal analysis*

The mechanical properties determining the performance of RC structural member under elevated temperatures are compressive and tensile strength, modulus of elasticity, and stress–strain response of constituent materials [9,39]. The constitutive relationships of concrete (under compression and tension) exposed to fire are obtained from the study conducted by Aslani and Bastami [5], as most of the available constitutive relationships of concrete at elevated temperature are not reliable for determining the stress–strain relationships effectively. Moreover, the developed models are able to predict accurate results, which are in good agreement with the experimental test results. Therefore, the compressive and tensile strength of concrete under elevated temperature is obtained from the following expressions [5,11],

$$\sigma_{cT}^{'} = \sigma_{c}^{'}\begin{bmatrix} 1.012 - 0.0005T \le 1.0 & ; & 20\ ^{\circ}\mathrm{C} \le T \le 100\ ^{\circ}\mathrm{C} \\ 0.985 + 0.0002T - 2.235\times10^{-6}T^{2} + 8\times10^{-10}T^{3} & ; & 100\ ^{\circ}\mathrm{C} < T \le 800\ ^{\circ}\mathrm{C} \\ 0.44 - 0.0004T & ; & 900\ ^{\circ}\mathrm{C} < T \le 1000\ ^{\circ}\mathrm{C} \\ 0 & ; & T > 1000\ ^{\circ}\mathrm{C} \end{bmatrix} \tag{34}$$

$$\sigma_{tT}^{'} = \sigma_{t}^{'}\begin{bmatrix} 1.05 - 0.0025T \le 1.0 & ; & 20\ ^{\circ}\mathrm{C} \le T \le 100\ ^{\circ}\mathrm{C} \\ 0.8 & ; & 100\ ^{\circ}\mathrm{C} < T \le 200\ ^{\circ}\mathrm{C} \\ 1.02 - 0.0011T \ge 0 & ; & 200\ ^{\circ}\mathrm{C} < T \le 800\ ^{\circ}\mathrm{C} \end{bmatrix} \tag{35}$$

where, σ'_c and σ'_{cT}, and σ'_t and σ'_{tT} are the compressive and tensile strengths of cylinder at ambient and elevated temperature, T, respectively. The elastic modulus at elevated temperature, E_{ciT} is similarly affected by the factors that influence the compressive strength, which is determined by the following expressions [5],

$$E_{ciT} = E_{ci}\begin{bmatrix} 1.0 & ; & 20\ ^{\circ}\mathrm{C} \le T \le 100\ ^{\circ}\mathrm{C} \\ 1.015 - 0.00154T + 2\times10^{-7}T^{2} + 3\times10^{-10}T^{3} & ; & 100\ ^{\circ}\mathrm{C} < T \le 1000\ ^{\circ}\mathrm{C} \\ 0 & ; & T > 1000\ ^{\circ}\mathrm{C} \end{bmatrix} \tag{36}$$

Table 4
Mechanical and thermal properties of concrete at ambient temperature.

	Parameters	Value
Mechanical properties	Compressive strength of concrete (f_c)	30 MPa
	Elastic modulus of concrete (E_c)	27386.12 MPa
	Coefficient of thermal expansion (α_c)	6.16×10^{-6} /°C
Thermal properties	Density (ρ_c)	2400 kg/m^3
	Conductivity (λ_c)	1.95 W/(m K)
	Specific heat (c_c)	913.22 J/(kg K)

The constitutive relations for concrete at elevated temperature to be used for design of structures under fire loading are limited in codes and standards. In the structural design, the stress–strain curve as a function of temperature in idealized form are expressed by the following equations [5],

Table 5
Mechanical and thermal properties of reinforcing steel at ambient temperature.

	Parameters	Value
Mechanical properties	Yield strength of steel (f_y)	415 MPa
	Ultimate strength of steel (f_u)	621 MPa
	Coefficient of thermal expansion (α_s)	1.15×10^{-5}/°C
Thermal properties	Elastic modulus of steel (E_y)	2×10^5 MPa
	Density (ρ_s)	7850 kg/m^3
	Conductivity (λ_s)	53.34 W/(m K)
	Specific heat (c_s)	J/(kg K)

$$\frac{\sigma_{cT}}{\sigma'_{cT}} = \frac{\beta_{mT}\left(\frac{\varepsilon_{cT}}{\varepsilon_{max}}\right)}{\beta_{mT} - 1 + \left(\frac{\varepsilon_{cT}}{\varepsilon_{max}}\right)^{\beta_{mT}}} \tag{37}$$

$$\varepsilon_{max} = 2\sigma'_c/E_{ci} + 0.21 \times 10^{-4}(T-20) - 0.9 \times 10^{-8}(T-20)^2 \tag{38}$$

$$\beta_{mT} = \beta_{mT,a}(\text{fitted}) = \left[1.02 - 1.17\left(E_{pi}/E_{ci}\right)\right]^{0.74};\ \varepsilon_{cT} \le \varepsilon_{max} \tag{39a}$$

$$\beta_{mT} = \beta_{mT,d}(\text{fitted}) = \beta_{mT,a}(\text{fitted}) + (a + 28b);\ \varepsilon_{cT} > \varepsilon_{max} \tag{39b}$$

where, $a = 2.7 \times (12.4\text{–}1.66 \times 10^{-2}\sigma'_{cT})^{-0.46}$ and $b = 0.83 \times \exp(-911/\sigma'_{cT})$, β_{mT} is a material parameter depending on the shape of the stress–strain curve, E_{ci} is the initial tangent modulus at ambient temperature, E_{pi} is the secant modulus at peak stress, ε_{cT} is the strain at temperature, T, ε_{max} is the strain at peak stress at temperature, T, and a and b are fitting parameters of the stress–strain curve.

The strength of concrete in tension is much lower than its compressive strength; hence, the tensile strength calculations are neglected at ambient and elevated temperatures. However, from the point of view of fire resistance, the tensile strength is important due to the development tensile stresses and progression of micro-cracking. The constitutive relation of concrete under tension at elevated temperature is given by the following equation,

$$\sigma_{tT} = \begin{bmatrix} \varepsilon_{ct}E_{ciT} & ; & \varepsilon_{ct} \le \varepsilon'_{ctT} \\ \sigma'_{tT}\left(\varepsilon'_{ctT}/\varepsilon_{ct}\right)^{0.75} & ; & \varepsilon_{ct} > \varepsilon'_{ctT} \end{bmatrix} \tag{40}$$

where, ε'_{ctT} is the tensile strain at peak stress. Finally, Fig. 3 is presented to illustrate the mechanical behavior of concrete under compression and tension for the cascaded fire analysis.

The degradation in mechanical properties of reinforcing steel, such as, yield strength and modulus of elasticity is considered to be vital parameter affecting the thermal performance of the structural members. For the present scenario, the stress–strain curve as well as the coefficients of degradation for elastic modulus and yield strength at elevated temperature is determined from the well-established guidelines of Eurocode, EC2 Part-1-2 [23]. The mechanical and thermal properties of concrete and steel at ambient temperature are shown in Tables 4 and 5.

4. Loading scenarios

4.1. Blast load scenario

A terrorist bombing scenario, representing a common case of detonation, is generally considered to simulate blast load in a typical structure, in which a blast pressure wave is generated to introduce the effects of blast and its high loading rate in the structure [15,27,28]. The generated blast wave generally encounters a rigid surface before incident on a structure and, in this regard, the obtained reflected pressure becomes significantly higher than the incident peak pressure. The RC structural member is analyzed under the application of the blast pressure, considering reflected peak pressure (P_r) from ground. Under surface blast scenario, the generated pressure due to ground reflection is generally incorporated by multiplying the charge weight by 1.7 to 1.8 [30,37]. Several relationships are available until the date to compute the amplified peak reflected blast pressure and the corresponding blast pressure history [26]. For the present study, empirical relationships provided by Kinney and Graham [38] are used, which involves incident pressure (P_{pos}) and positive phase duration (t_{pos}) to compute blast overpressure history. Thus, the incident pressure and positive phase duration are obtained as,

Table 6
Blast and fire loading parameters.

	Parameters	Unit	Values
Blast loading	Charge weight (W)	kg	200
	Standoff distance (S)	m	15
	Scaled distance (Z)	kg/m$^{1/3}$	2.65
	Scaling factor due to ground	–	1.8
	Scaling factor due to incident angle	–	2.5
	Peak reflected pressure (P_r)	kPa	207.824
	Arrival time (t_a)	ms	9.04
Fire loading	Thermal inertia (b)	J m^{-2} °C^{-1} s$^{-1/2}$	1800
	Fire load density (q)	MJ/m^2	780
	Duration of fire loading (d_f)	hour	2
	Opening factor (O)	m$^{1/2}$	0.075
	Fire growth (t_{lim})	min	Slow (25)
	Convection (exposed)	W/(m^2 K)	35
	Radiation/ emissivity	–	0.8

$$P_{pos} = \frac{P_0 \times 808 \times \left[1 + \left(\frac{Z}{4.5}\right)^2\right]}{\sqrt{\left[1 + \left(\frac{Z}{0.048}\right)^2\right] \times \left[1 + \left(\frac{Z}{0.32}\right)^2\right] \times \left[1 + \left(\frac{Z}{1.35}\right)^2\right]}}\,(\text{bar}) \tag{41}$$

$$t_{pos} = \frac{W^{1/3} \times 980 \times \left[1 + \left(\frac{Z}{0.54}\right)^{10}\right]}{\sqrt{\left[1 + \left(\frac{Z}{0.02}\right)^3\right] \times \left[1 + \left(\frac{Z}{0.74}\right)^6\right] \times \left[1 + \left(\frac{Z}{6.9}\right)^2\right]}}\,(\text{ms}) \tag{42}$$

where, W is charge weight (in kilograms) in terms of the mass of equivalent trinitrotoluene (TNT), $Z = R/W^{1/3}$ is scaled distance, and P_0 is the atmospheric pressure. The radial distance R is defined as a distance from the point of consideration to the source of detonation. Therefore, considering the abovementioned parameters, the time history of pressure wave at any time instant is expressed as [7],

$$P(t) = P_0 + P_{pos}\left(1 - t/t_{pos}\right)\exp\left(-bt/t_{pos}\right) \tag{43}$$

where, t is time measured after arrival time, t_a, which is assumed as 0, and $b = Z^2\text{-}3.7Z + 4.2$ is unitless decay parameter [42]. The peak reflected pressure, $P_r = C_r P_{pos}$ is computed using the coefficient of reflection (C_r) charts provided in the Unified Facilities Criteria (UFC) 3-340-02 [66]. Finally, the blast loading parameters are presented in Table 6 based on the empirical relations given above.

4.2. Fire load scenario

The coupled thermo-mechanical analysis considering pre-damage from the previous blast analysis is conducted by providing thermal boundary conditions to the surface of interest in the RC structural member [12]. In order to simulate thermal behavior in the RC structure, a realistic fire curve is obtained using the prescribed recommendations in the EC1 [22]. The realistic fire curve comprises of two parts: (i) heating phase and (ii) cooling phase. The time–temperature curve for the heating phase is given as,

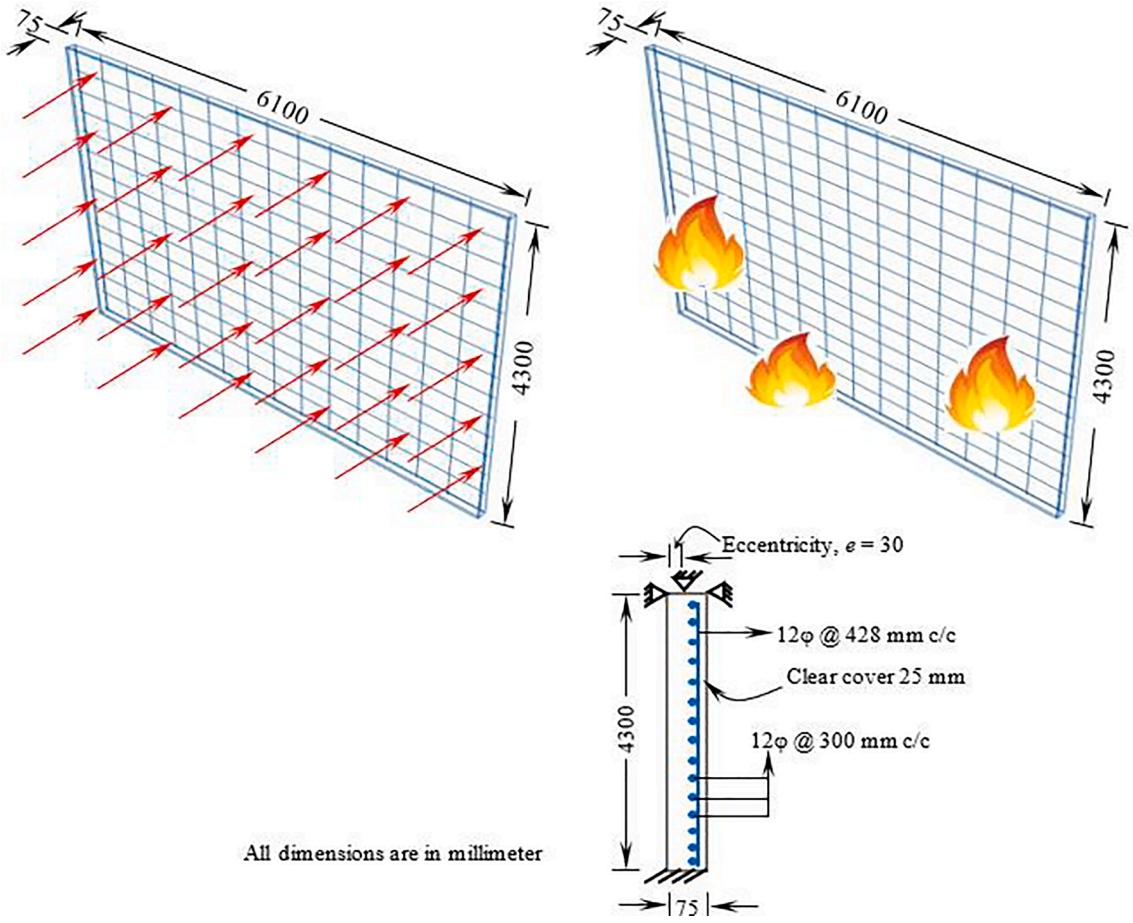

Fig. 4. 3-D view showing blast and fire exposure, and sectional cross-section view showing boundary conditions and reinforcement details of the RC panel.

$$T = 20 + 1325\left(1 - 0.324e^{-0.2t^*} - 0.204e^{-1.7t^*} - 0.472e^{-19t^*}\right) \quad (44)$$

where, T is temperature obtained during the heating phase, and $t^* = t\Gamma$ is determined in seconds. The parameter Γ depends on opening factor, O and thermal inertia, b-factor, which is given by,

$$\Gamma = (O/b)^2 \Big/ (0.04/1160)^2 \quad (45)$$

where, $b = \sqrt{(\rho_c c_c \lambda_c)}$ is the thermal inertia of concrete, ρ is density of concrete, c_c is specific heat capacity, and λ_c is thermal conductivity mainly used to characterize the thermal properties of the concrete material. The duration of heating phase is given by,

$$t_{max} = \max\left\{\left(0.2 \times 10^{-3} \times q/O\right), t_{lim}\right\} \quad (46)$$

where, q is fire load density (MJ/m^2) considered in the design depending on occupancy of building. According to the code recommendations, t_{lim} for slow, medium, and fast fire growth rate are 25 min, 15 min, and 10 min, respectively. Likewise, the temperature for cooling phase is given as,

$$T = T_{max} - 625\left(t^* - t^*_{max}x\right) \quad \text{for} \quad t^*_{max} \le 0.5 \quad (47a)$$

$$T = T_{max} - 250\left(3 - t^*_{max}\right)\left(t^* - t^*_{max}x\right) \quad \text{for} \quad 0.5 < t^*_{max} < 2 \quad (47b)$$

where, $t^*_{max} = t_{max}\Gamma$, $x = 1$ for $t_{max} > t_{lim}$ and $x = t_{lim}\Gamma/t^*_{max}$. Lastly, the fire loading parameters are presented in Table 6 along with the blast loading parameters based on the empirical relations given in the EC1 [22].

In the current study, fire resistance rating of the RC structural member is obtained using the natural fire curve discussed above, although, the fire rating is based on standard fire curve prescribed by the ISO 834 [32], which uses idealized time–temperature curves. The standard fire curves are relatively simpler compared to the natural fire curve, although the accuracy involved in the fire severity has drawn much criticism. On the other hand, natural fire curves recommended in the EC1 [22] are advanced and realistic; however, no standard guidelines exist for using these advanced time–temperature curves to determine the fire resistance of structure. Nevertheless, researchers recently have been using the EC1 parametric fire curves to determine the performance and resistance of structural members [29,59]. This is based on existence of uniform temperature in small to medium compartments, unlike in large compartments. The same assumption is difficult to incorporate in the large compartments due to existence of considerable differences between the uniform and non-uniform fires [58]. Hence, in the present study, parametric fire curve prescribed in the EC1 [22] is used to determine the fire resistance of the pre-damaged RC structural member under fire.

Table 7
Accidental eccentricity and mechanical load assumed for the analysis.

RC Panel	Thickness (mm)	Accidental eccentricity (mm)	Mechanical load (kN/m^2)	
			Dead load	Live load
Wall panel	75 100 125	30 mm towards the direction of blast and fire exposure	107.5	320

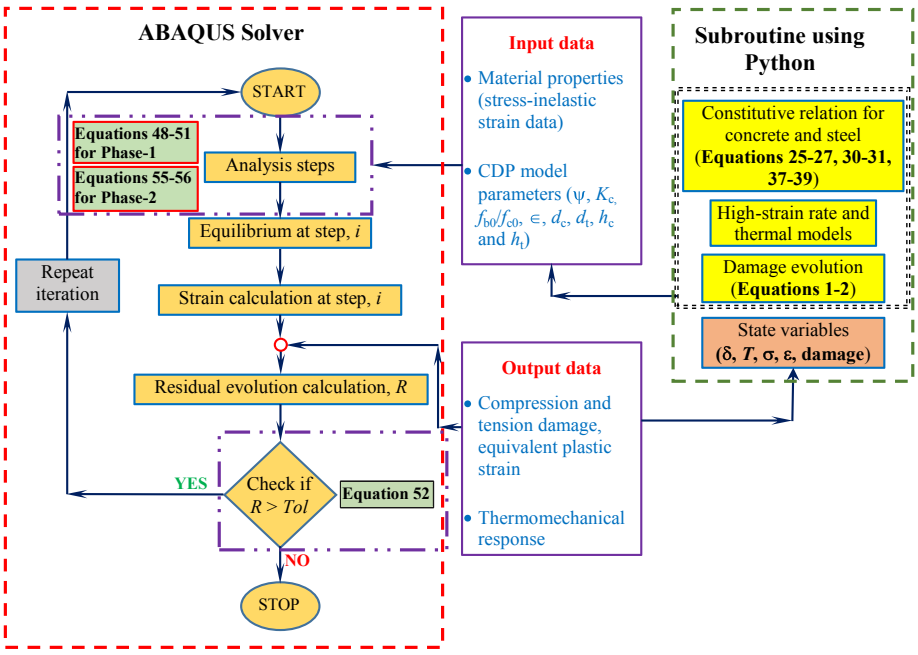

Fig. 5. Framework for linking Python-programming interface and the ABAQUS® solver.

5. Finite element (FE) modeling approach

5.1. Structural description and detailing

Herein, a 3-dimensional (3-D) RC structural member is investigated under the cascaded fire scenario considering pre-damage of the RC member under a blast scenario. Note that, through such 3-D modeling, temperature-dependent Poisson's effects are duly catered for [13]. The RC structural member adopted for the study is a RC wall panel member considering different thicknesses, wherein the structural elements of different thicknesses are first exposed to blast scenario, and subsequently the pre-damaged structure is exposed to cascaded fire scenario. The RC panels used for the study have similar planar dimension of 6.1 m × 4.3 m with varying thicknesses of 75 mm, 100 mm, and 125 mm, and the considered RC panels are assumed to be 4.3 m high, as shown in Fig. 4. The RC panel under compressive in-plane load illustrates a typical load-bearing wall subjected to axial load at certain eccentricity, which denotes accidental eccentricity during application of service load on the RC wall. Each structural panel is embedded with a single layer of steel reinforcement in concrete having clear cover of 25 mm on tension side. Along the longitudinal direction, each panel, irrespective of loading conditions, is reinforced with 12φ steel rebar spaced at 428 mm center-to-center (c/c) on the tension side, where φ represents the diameter of rebar in mm. Similarly, along the transverse direction, each RC panel is reinforced with 12φ rebar spaced at 300 mm c/c on both sides, as shown in Fig. 4. The mechanical loads applied on each RC panels are calculated from the dead load (DL) and live load (LL). The mechanical loads are treated as axial compressive in-plane force, which are calculated from the dead loads of beam and slab, and imposed load of slab. The mechanical loads and accidental eccentricity assumed for each RC wall panel under the compressive in-plane load are provided in Table 7. Finally, the RC panels are not specifically designed to resist any accidental blast or fire loads, nor any fire resisting material is applied on each panel; except that the code-prescribed concrete cover is provided.

5.2. FE model of RC wall panel

The behavior of the 3-D RC wall panels subjected to cascaded fire loading after exposure to the blast is studied by developing finite element (FE) models of each RC wall panel using Python scripts, linked with commercially available software ABAQUS® [1], employed as a solver. An analysis framework has also been developed in the form of a flowchart (Fig. 5) to present an essential link between the Python programming interface and ABAQUS® solver employed in the present study. The FE model of each RC wall is developed by 3-D part using extrusion feature, in which a single layer of steel reinforcement is provided perpendicular to each other on tension face maintaining a concrete clear cover assumed from Indian standard, IS 456 [31]. Nonlinearity in concrete is introduced using the concrete damaged plasticity (CDP) model taking into account the degradation of the elastic stiffness induced by plastic strains in both tension and compression. The CDP model is also capable to model dowel action between concrete and steel rebar using suitable tension stiffening parameters. The axial forces are transferred through steel reinforcement, which is modeled using the classical theory of metal plasticity. Full bonding is assumed between steel rebar and concrete, which is achieved using tie constraint option.

The cascaded thermo-mechanical analysis of each RC wall panel subjected to pre-damage under blast loading is conducted in two phases, viz., Phase-1 and Phase-2. Dynamic stress analysis is conducted in Phase-1 under the considered peak reflected pressure generated from the blast loading scenario. The cascading fire analysis is conducted in Phase-2 considering the induced mechanical loadings as well as the pre-damaged condition of the RC wall panel exposed to the blast loading. The pre-damage effect is simulated by importing the pre-damage state of the RC wall from Phase-1, which considers the degradation of mechanical properties induced in the materials. The pre-damage effect is simulated using pre-defined field option available in the ABAQUS® solver. In this option, last step of the previous Phase-1 blast analysis is used as an initial state to simulate the pre-damaged behavior of the RC panel for the subsequent Phase-2 coupled thermo-mechanical analysis. It must be noted that the use of predefined field becomes relatively limited when there is a change in geometry in both the phases.

Coupled temperature-displacement continuum C3D8RT element with reduced integration is used to lump the mesh of concrete geometry in both the phases. Each node of a C3D8RT element has 4 degree of freedoms (DOFs), three translational DOFs (1, 2, 3) in mutually perpendicular directions, x, y, z, and a temperature DOF (11), where the x and y directions are in-plane, whereas the z direction is normal to the

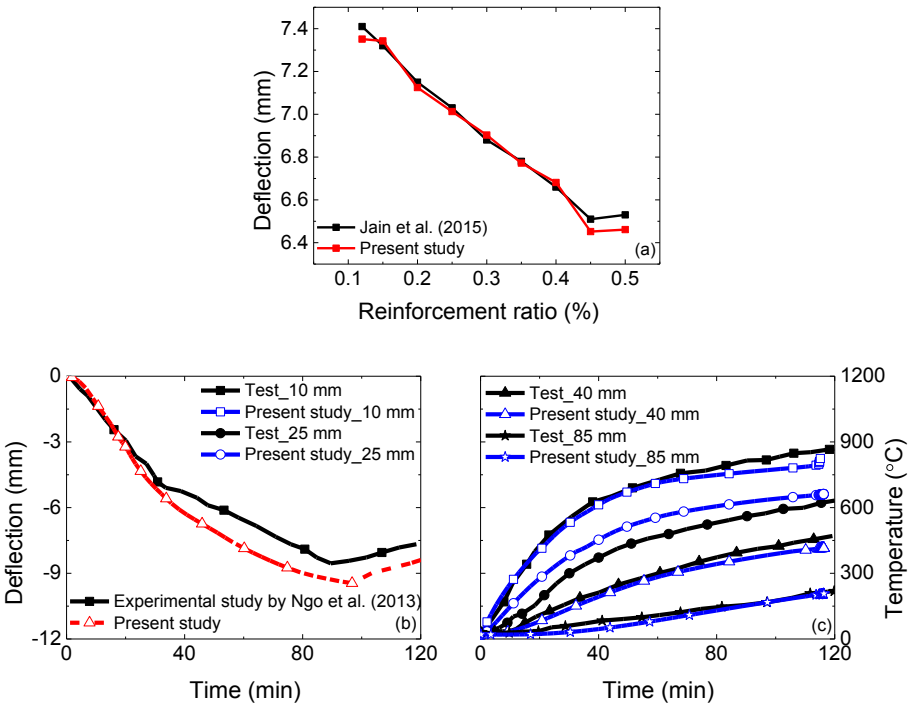

Fig. 6. Validation of independent RC wall panels under fire and blast scenarios.

wall. Here, DOFs (1, 2, 3, and 11) are standard notations used in ABAQUS® solver. As the C3D8RT element has DOFs 1, 2, 3, and 11, DOF 11 is suppressed for Phase-1 dynamic stress analysis; whereas, in the subsequent Phase-2 coupled temperature-displacement analysis, DOF 11 is allowed for the temperature DOF. The mesh of the steel rebar geometry is lumped by truss element T3D2T in both the phases, which includes a temperature DOF for the cascaded thermo-mechanical analysis. Embedded constraint available in ABAQUS® solver is used in Phase-1 to constrain the translational degrees of freedom of the embedded nodes (steel reinforcement) to transfer the stresses from concrete to steel rebar through the developed nodes. Tie constraint feature is used in Phase-2 to constrain the nodes of the concrete and steel interface to allow the temperature distribution from concrete to the steel. Each RC wall is fixed at the bottom and clamped on other three sides. The boundary conditions in each RC wall panel are given as: (i) bottom face: DOFs – u_x (1) = u_y (2) = u_z (3) = ϕ_x (4) = ϕ_y (5) = ϕ_z (6) = 0, and (ii) remaining sides: DOFs – u_x (1) = u_y (2) = u_z (3) = 0.

The thermal loading on the structural panels is applied as convection and radiation boundary conditions at the desired surface of exposure, as shown in Fig. 4. A convective heat transfer coefficient in the form of a surface film condition is applied at the exposed surface of panels assuming that no heat is transferred through the unexposed side of the panels. The radiation boundary condition is given in terms of emissivity coefficient. Here, the convective heat transfer and radiation coefficient adopted for simulating the thermal loading is assumed as 35 W/(m^2 K) and 0.8, respectively. The entire RC panels under mechanical loading scenarios are subjected to an ambient temperature of 20 °C in the form of predefined initial condition. The thermo-mechanical analysis is carried out for a duration of 120 min and the response at each node is stored for post-processing. The mesh size is determined by convergence trials indicating no influence in the obtained numerical results on further decreasing the element size.

5.3. Numerical solution scheme

The numerical solution approach and solution schemes are divided for two different phases as mentioned, Phase-1: explicit dynamic analysis and Phase-2: coupled displacement-temperature analysis. The blast analysis is performed using the dynamic explicit procedure present in ABAQUS® solver domain. The solver performs dynamic analysis using explicit central difference integration scheme. The solution obtained in final step of Phase-1 is used as initial state for the subsequent Phase-2, which is aimed to investigate the coupled thermo-mechanical responses of the pre-damaged RC wall subjected to high strain-rate induced by the blast loading. The numerical techniques used for coupled thermo-mechanical analyses in Phase-2 are finite difference method (FDM) discretization and finite element method (FEM) spatial approximation. The solution schemes used to assess the RC wall panels under the individual dynamic blast and coupled thermal and mechanical loading is discussed hereunder.

The dynamic analysis of the RC wall panels under the blast loading is performed in explicit domain as it is more efficient for solving wave propagation problems, whereas, the standard domain in ABAQUS® is found more efficient for solving smooth nonlinear thermo-mechanical problems. In both explicit and standard domains, the nonlinear response is obtained incrementally. The discretized equilibrium equation in FE environment is expressed as,

$$\{P\}^t - \{I\}^t = [M]\{\ddot{u}\}^t \tag{48}$$

where, $\{P\}^t$ is the external force vector, $\{I\}^t$ is the internal force vector created from element stresses, $[M]$ is the diagonal lumped nodal mass matrix, $\{\ddot{u}\}^t$ is the nodal acceleration at beginning of the increment, and $[M]\{\ddot{u}\}^t$ is the force vector due to the material inertia. Therefore, the nodal acceleration can be obtained as under,

$$\{\ddot{u}\}^t = [M]^{-1}\left(\{P\}^t - \{I\}^t\right) \tag{49}$$

Central difference integration scheme is used to update the velocity and displacement at each node from Eq. (49), which is expressed as,

$$\{\dot{u}\}^{t+\frac{\Delta t}{2}} = \{\dot{u}\}^{t-\frac{\Delta t}{2}} + \left(\frac{\Delta t^{t+\Delta t} + \Delta t^t}{2}\right)\{\ddot{u}\}^t \tag{50}$$

$$\{u\}^{t+\Delta t} = \{u\}^t + \Delta t^{t+\Delta t}\{\dot{u}\}^{t+\frac{\Delta t}{2}} \tag{51}$$

Iterations are not required in equation solver to update the

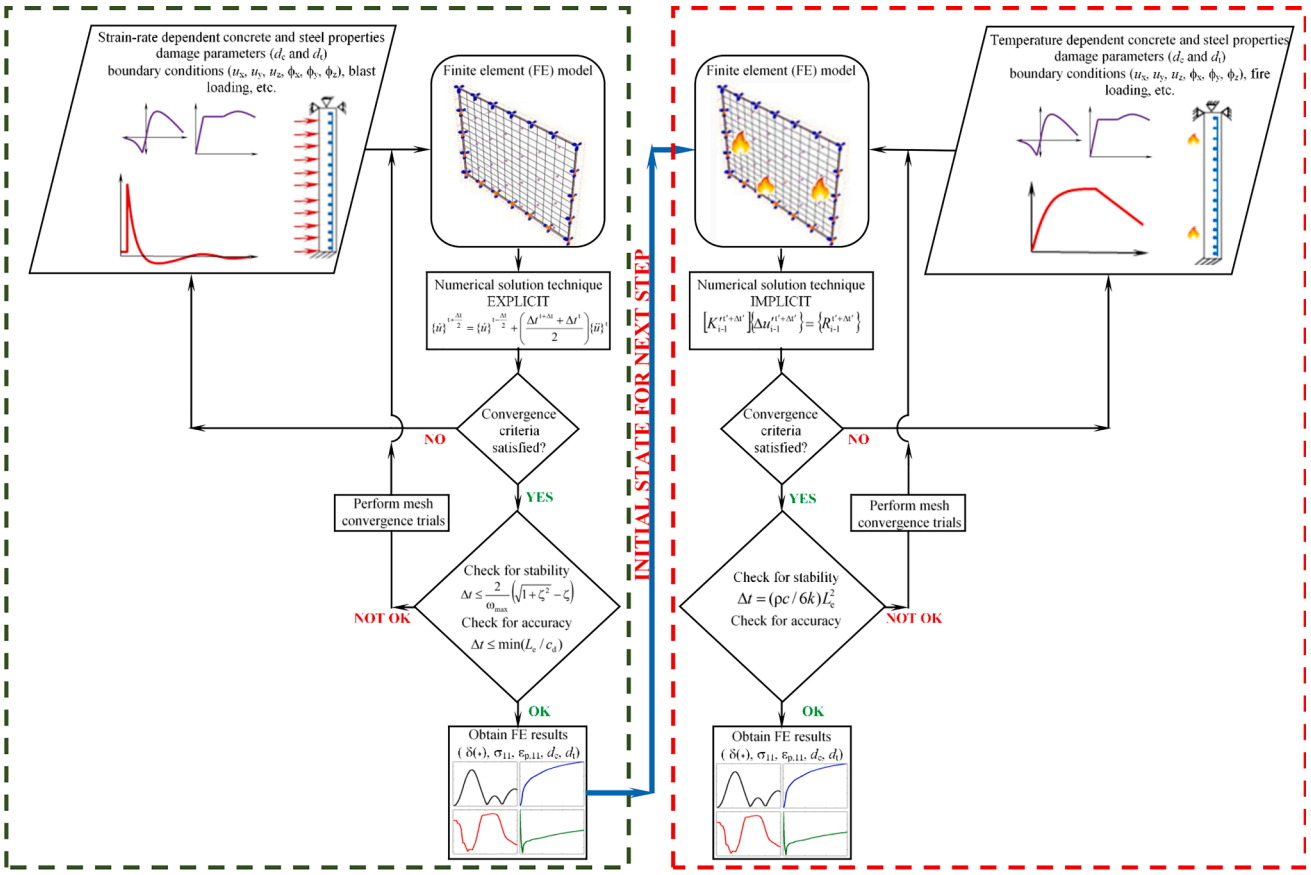

Fig. 7. Flowchart showing the procedure followed in analyzing the cascading hazard analysis for the RC wall panel.

acceleration, velocity, and displacement responses. The analysis using explicit operator is performed using a large number of time-increments of small size. However, the central difference integration scheme is conditionally stable, and the solution becomes unstable and diverges rapidly if the time increment is too large. In this regard, stability limit for the operator in terms of Eigen value is given by,

$$\Delta t \le \frac{2}{\omega_{max}}\left(\sqrt{1+\zeta_d^2}-\zeta_d\right) \tag{52a}$$

where, ω_{max} represents maximum Eigen value of the element, and ζ_d represents fraction of critical damping at the highest mode. Here, the purpose of introducing damping for the response solution is to merely reduce the stable time increment, wherein a small amount of damping is required to be introduced in the form of bulk viscosity to control high frequency oscillations. The bulk viscosity does not influence the stress parameters because it is incorporated as a numerical effect and not as a part of constitutive response for material. The bulk viscosity is based on the dilatational mode of each element and the fraction of critical damping each element is given by,

$$\zeta = b_1 - b_2^2 \frac{L_e}{C_d}\min(0, .\varepsilon_{vol}) \tag{52b}$$

where, b_1 and b_2 are damping coefficients having values of 0.06 and 1.2, respectively, L_e is characteristic length of the smallest element in the domain, $c_d = \sqrt{\frac{\widehat{\lambda}+2\widehat{\mu}}{\rho}}$ is the dilatational wave speed, $\dot{\varepsilon}_{vol}$ is the volumetric strain-rate, $\widehat{\lambda}$ is the first Lamé constant, $\widehat{\mu}$ is the shear modulus, and ρ^* is the density of the element, chosen automatically to satisfy the user-defined critical time step. The stable time increment can be expressed as, $\Delta t \le \min(L_e/c_d)$. Hence, it is worthwhile to conduct mesh convergence trials to have insignificant influence on the numerical results without substantially increasing the computation time.

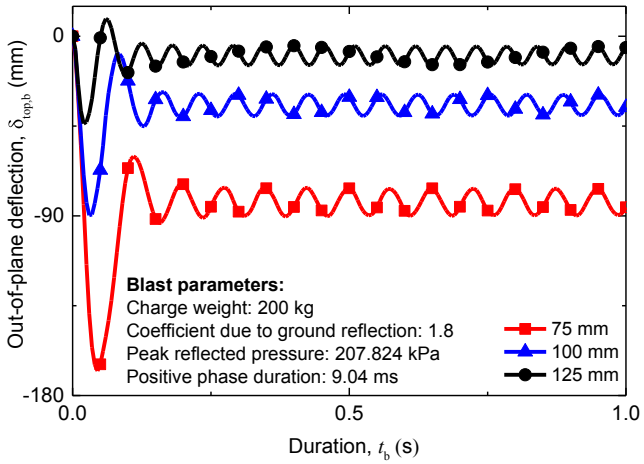

Fig. 8. Displacement time history at center of the RC wall panels under dynamic blast loading.

In the subsequent coupled temperature-displacement analysis (Phase-2) for the RC wall panel, the temperature history is applied to the exposed surface of the RC wall through convection and radiation considering pre-damage induced by the blast loading. The heat is transferred within the RC wall by means of heat conduction; and, heat transferred to the wall is through heat convection and radiation mechanisms. The transient heat conduction equation along with the boundary condition and the convection condition can be expressed as,

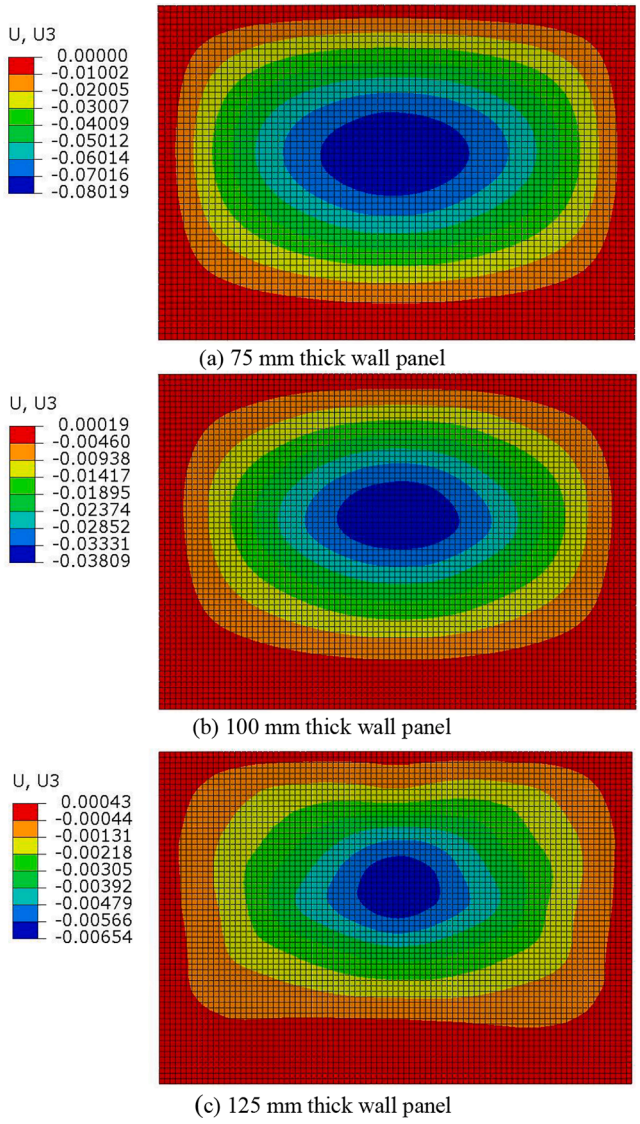

Fig. 9. Displacement (in m) profile of the RC wall panels under the blast scenario.

$$Q = \rho c \frac{\partial T}{\partial t} - \nabla \cdot (k \nabla T) \tag{53}$$

$$(-k\nabla T)\cdot n = H_c\left(T_f^4 - T_c^4\right) \tag{54}$$

where, Q is overall heat transferred from outside, ρ* is density of material (kg/m^3), c* and k* are the specific heat capacity (J kg^{-1} K^{-1}) and thermal conductivity (W m^{-2} K^{-1}) respectively, for concrete or steel, n is unit vector outer normal to the boundary, H_c is convective heat transfer coefficient, and T_f and T_c are ambient temperature and temperature at reference surface, respectively. From the equation, it can be observed that the transient conduction problem follows parabolic relation with time dependence and elliptic behavior with spatial coordinates.

The implicit nonlinear FE solution technique uses backward finite difference algorithm to integrate the governing equations in time domain. The thermal field is solved in each time step, Δt, and subsequently the mechanical problem is solved using the obtained thermal strains. The tolerances on residual errors need to be satisfied in every iteration before proceeding to the next time step. The nonlinear system of equations is approximated as linear within each time step and are solved using the Newton-Raphson iteration scheme for static equilibrium. The technique requires several global equilibrium iterations, which can be written as under,

$$\left[K^{t+\Delta t}_{i-1}\right]\left\{\Delta u^{t+\Delta t}_{i-1}\right\} = \left\{R^{t+\Delta t}_{i-1}\right\} \tag{55}$$

where, $\left\{\Delta u^{t+\Delta t}_{i-1}\right\}$ is an incremental change to the vector solution, expressed in terms of temperature and displacements in thermo-mechanical problems, $\left[K^{t+\Delta t}_{i-1}\right]$ is the tangent stiffness matrix also known as the material Jacobian [J], and $\left\{R^{t+\Delta t}_{i-1}\right\}$ is the residual error vector obtained from the external and internal force vectors. Further, on solving Eq. (55) for $\left\{\Delta u^{t+\Delta t}_{i-1}\right\}$, convergence at the next time step, $t + \Delta t$ is checked and subsequently updated by Eq. (56) written as follows,

$$\left\{u^{t+\Delta t}_{i}\right\} = \left\{u^{t+\Delta t}_{i-1}\right\} + \left\{\Delta u^{t+\Delta t}_{i-1}\right\} \tag{56}$$

The standard solver uses automatic increment by default and rate of convergence in each time step is monitored to determine the appropriate time and load increments. However, minimum usable time increment as a function of element length can be estimated using $\Delta t = (\rho c/6k)\Delta L_e^2$, as employed here. Moreover, it is to be ensured that local instabilities, such as material instability or local buckling are not developed throughout the phases of the analyses. In such cases, damping is introduced throughout the model in such a way that the generated viscous forces are sufficiently large to prevent instantaneous buckling without altering the stability. Here, the damping factor is calculated using iterations based on the dissipated energy fraction. In the present study, 'automatic stabilization scheme' with a constant damping factor available in ABAQUS® is used to typically subside the instabilities and to eliminate rigid body modes without having a major effect on the solution.

It is critical to note that in such explicit nonlinear simulations in Phase-1 where the structural elements undergo very large deformations and distort the FE mesh ending in a point of providing inaccurate results due to numerical reasons, it is necessary to increase the mesh size to minimize the distortion in the structure. On contrary, for implicit nonlinear simulation technique in Phase-2, the increment size depends on the rate of convergence and in such highly nonlinear problems due to slow convergence, the increment size needs to be decreased. Therefore, the mesh size in the RC wall geometry is chosen appropriately to counter the extreme nonlinearity under both the extreme hazards, viz., high strain-rate blast and the subsequent thermo-mechanical loadings.

6. Validation study

The modeling strategy used in the present study is independently validated by comparing the results from the studies conducted by Jain et al. [33] and Ngo et al. [55] for the blast and fire analyses, respectively.

A three-dimensional (3-D) FE model is developed for a square RC wall having dimensions 2 m × 2 m with thickness of 200 mm, as analyzed by Jain et al. [33]. The FE model is developed using 3-D part option in ABAQUS®, in which a single layer or single mat of two-way steel reinforcement, perpendicular to each other is provided in which a concrete clear cover of 75 mm according to [31]. The layers of reinforcements are created as separate part and assembled using embedded option to assume full bonding and further transfer the stresses from concrete to steel. The CDP model is used to simulate stress–strain behavior in concrete for both strain-rate-dependent and rate-dependent stimulations. The steel reinforcement is modeled using the plasticity model for strain-rate-dependent simulations. The RC panel is modeled using 3-D continuum 8-node linear brick element (C3D8R) with reduced integration, and hourglass control. The steel rebar is modeled using 2-node linear 3-D truss (T3D2) element. All four sides of the concrete walls are restrained in three Cartesian directions, i.e., x, y, and z. The interaction between concrete and the rebar is modeled with the embedded region option available in the ABAQUS®. Blast load is simulated as an equivalent triangular pressure pulse calculated using

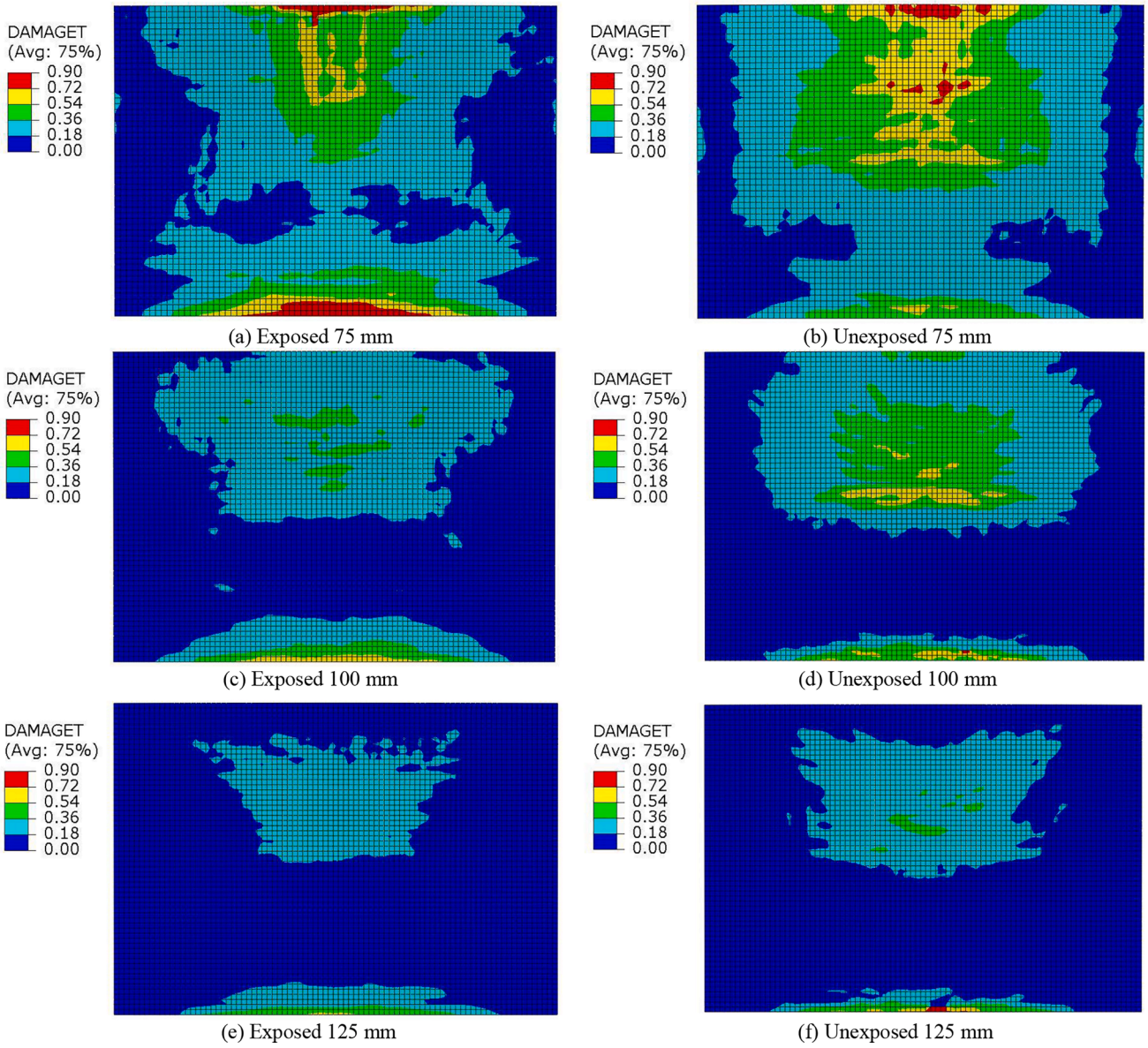

Fig. 10. Tensile damage (d_t) at the exposed and unexposed faces of the RC wall panels under the blast loading.

UFC 3-340-02 [66].

The analyses are performed for a peak blast overpressure of 1.162 MPa, with wave arrival time as 1.59 ms, and positive phase duration as 6.14 ms. The study is conducted for total step time of 7 ms, and the results are compared with the study published by Jain et al. [33]. The concrete grade for the current study is taken as M25, i.e., with characteristic compressive strength of 25 MPa. The Young's modulus (E), Poisson's ratio (μ), and mass density (ρ) assumed for concrete are taken from the published work. The tensile strength of concrete is calculated as $0.7\sqrt{f_{ck}}$. The steel reinforcement used is Fe415 grade steel with static tensile yield stress, $\sigma_t = 415$ MPa. The model is validated, and the results obtained in the present study are compared with the published results. The comparison of the results is shown in Fig. 6(a). It is observed that the displacement response increases upon decreasing the reinforcement ratio. The accuracy of the results is observed to be in range of 95–98%, which shows the validation of the adopted FE modeling strategy.

A nonlinear 3-D RC load-bearing wall is modeled in ABAQUS® environment having dimensions 1000 mm × 150 mm × 2400 mm, as conducted by Ngo et al., [55]. In the RC panel, eight vertical bars are provided as longitudinal reinforcement of 16φ; whereas, horizontal bars of 14φ are provided as lateral reinforcement with center-to-center (c/c) spacing of 300 mm with concrete clear cover of 25 mm. The characteristic compressive strength of the concrete used in the model is 31.8 MPa. The load-bearing wall is subjected to an axial load of 485 kN at an eccentricity of 10 mm towards the fire loading. The eccentricity represents typical accidental eccentricity caused due to construction imperfections, geometry, etc. The load-bearing wall is analyzed for simply-supported conditions at top and bottom surface. A 2-h duration standard fire curve as per ISO 834 [32] is used to simulate the behavior of fire in the wall with single-side exposure. The thermo-mechanical analysis is carried out using C3D8RT element for concrete and T3D2T for rebar. The deflection response at the center as well as different interfaces of the wall is compared as shown in Fig. 6(b) and (c), which shows an accuracy of 97% in the obtained result. The obtained FE results are in good agreement with the experimental study conducted by Ngo et al. [55], which demonstrates the accuracy of the modeling technique adopted.

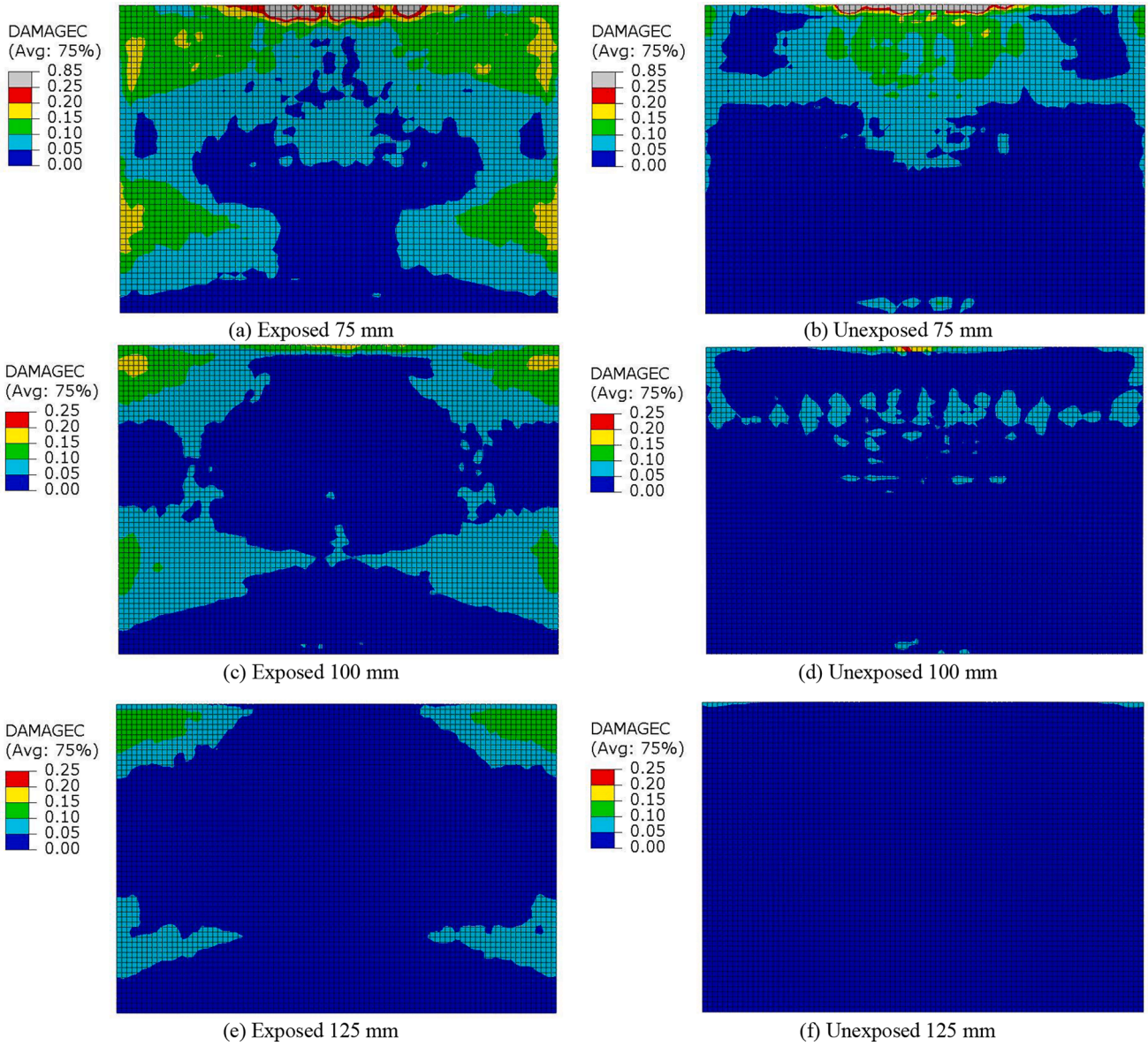

Fig. 11. Compressive damage (d_c) at the exposed and unexposed faces of the RC wall panels under the blast loading.

7. Numerical study

Herein, the 3-D RC panels are studied by first exposing to dynamic blast loading and then subsequently to cascaded fire loading. Each RC panel is investigated considering the effect of nonlinearity in material and geometric properties for blast and the subsequent cascaded fire loading. In the present study, for initial blast analysis, the amount of charge weight adopted is 200 kg placed at a stand-off distance of 15 m to analyze the effect of dynamic blast loading. The reflected pressure for this case is obtained as 519.560 kPa. However, extreme challenges were faced to solve the problem due to high nonlinearity under cascaded fire after considering pre-damage under the blast loading; hence, the reflected pressure load was reduced to 207.824 kPa for countering the extreme nonlinearity in the RC panels. The results for dynamic blast loadings discussed hereby are obtained for the peak reflected pressure of 207.824 kPa, which are then subsequently used for the cascaded fire analysis. The RC panels are subjected to blast and fire loadings exposed to single-side, which is opposite to the tension face, as shown in Fig. 4. Finally, the thermo-mechanical responses of the RC panels are studied in terms of deflection, distribution of temperature, evolution of damage, and plastic strain at the exposed and unexposed faces of the RC panels to understand the behavior and mechanism of damage evolved for the RC wall panels under the complex scenario. Eventually, Fig. 7 is presented to demonstrate the algorithm to conduct the cascading hazard analysis under post-blast fire scenario.

7.1. Results and discussion

Figs. 8 and 9 show the out-of-plane deflection of the wall panels exposed to surface blast scenario. The deflection increases with decrease in thickness of the RC panels. The highest deflection (174.96 mm) is observed for the 75 mm thick wall panel, whereas the lowest deflection (44.23 mm) is observed for the 125 mm thick panel. The peak deflection reduces by almost 100% upon increasing the thickness of the wall panels. However, the residual displacements do not follow the same trend. The mean residual deflection for the wall panels of thicknesses 75 mm, 100 mm, and 125 mm are observed to be 78 mm, 30 mm, and 8 mm, respectively. This shows that with proportional increase in

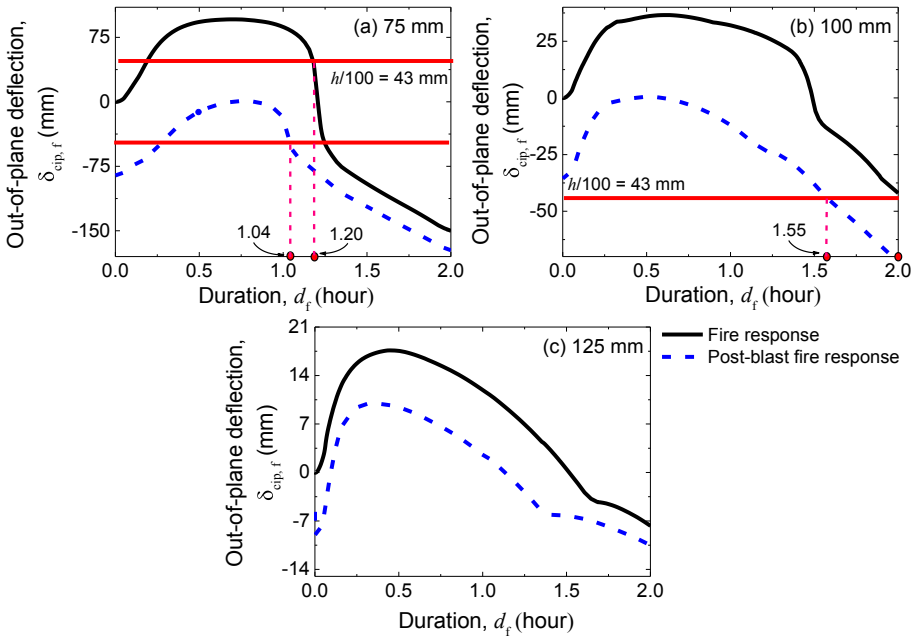

Fig. 12. Out-of-plane deflection at the center of the RC wall panels under traditional and post-blast fire.

thickness of the wall panel, the residual displacement reduces significantly. Therefore, it can be concluded that the wall panel of thickness 125 mm may be effectively used as a blast-resistant member for similar range of blast peak overpressure in the given scenario.

Fig. 10 shows the tensile damage (d_t) induced at the exposed and unexposed sides for the wall panels with different thicknesses under the surface blast scenario. The extent of d_t is relatively higher observed at the unexposed face as compared to the exposed face. This is because the mechanical loads in addition to the blast load generates more tensile stresses at the unexposed face. With increase in dynamic stresses, there is a relative increase in the plastic strains, which eventually is proportional to the damage induced. The induced damage reduces significantly with increase in thicknesses of the wall panels. The initial compressive wave of the blast load gets converted to tensile wave as the blast wave travels through the RC member, causing relatively higher extent of cracking at the unexposed side. Majority of damage induced is concentrated around the center of wall panels and relatively lesser damage is observed at bottom part of the wall panel. Upon observation in the central region of the exposed face of the wall panel, the damage is predominant from 18% to 72% for the 75 mm thick wall panel. The damage reduces significantly for the 100 mm thick wall panel as majority of the damage is concentrated between 18% and 36 % and marginal damage above 36%. Finally, the damage in 125 mm thick wall is the least and the damage level is observed from 18% to 36%. Similarly, the damages in the unexposed faces of the wall panels are also observed. The damage level in the central region of the unexposed face for the 75 mm thicker wall panel under the blast scenario is observed from 18% to 90%. The region with damage from 36% to 72% is comparatively more than the exposed surface. Similarly, significant damage from 36% to 72% is observed for the 100 mm thick wall panel, whereas, the 125 mm thick wall panel has also exceeded 36% damage.

Fig. 11 illustrates the compressive damage (d_c) induced at the exposed and unexposed faces of the wall panels under surface blast scenario. The unexposed faces do not undergo significant compressive damage as compared to the exposed faces, as compressive strains are induced at exposed faces subjected to the dynamic blast loading. The exposed faces of all panels do not exceed 25% damage as the generated compressive strains are relatively lesser. The unexposed face for the 125 mm thick wall panel hardly undergoes any damage. The damage levels indicate the development of plastic strains in the wall panels due to blast loadings; hence, it can be concluded that 125 mm RC wall panel may serve as better blast-resistant structural element in regions where blast overpressure of such range is expected in the scenario considered here.

Fig. 12 deals with the central out-of-plane deflections ($\delta_{cip,f}$) of the wall panels under the cascaded fire scenario, which are also compared with the deflections under normal fire scenario. The deflection profiles of the RC wall panels under the cascaded fire demonstrate significant difference in the behavior of the RC wall panels, which eventually affect the fire resistance of the panels. The deflection profile of the RC wall panels under normal thermo-mechanical loading depends on the application of the mechanical load, effect of boundary conditions, and thermal gradient generated due to temperature difference. Due to high thermal inertia of concrete, high thermal gradients are induced resulting in relatively higher expansion near the exposed face. This causes movement of the wall panel away from exposed face under compressive in-plane loading, which is known as thermal bowing, causing extensive horizontal out-of-plane displacement at the unexposed side. Now, with the occurrence of fire after the wall panels are inflicted with some degree of damage due to the blast loading, the structural panels undergo more severe damage under the cascaded fire loading. This is because the behavior of the wall panels under the post-blast fire is subsequently dependent on stiffness degradation from deformed geometry due to initial damage sustained by the walls. As a result, deflection profiles for the wall panels under the cascaded fire effect do not follow the same trend as compared to the wall panels under the normal fire scenario. The maximum responses of the 75 mm, 100 mm, and 125 mm wall panels

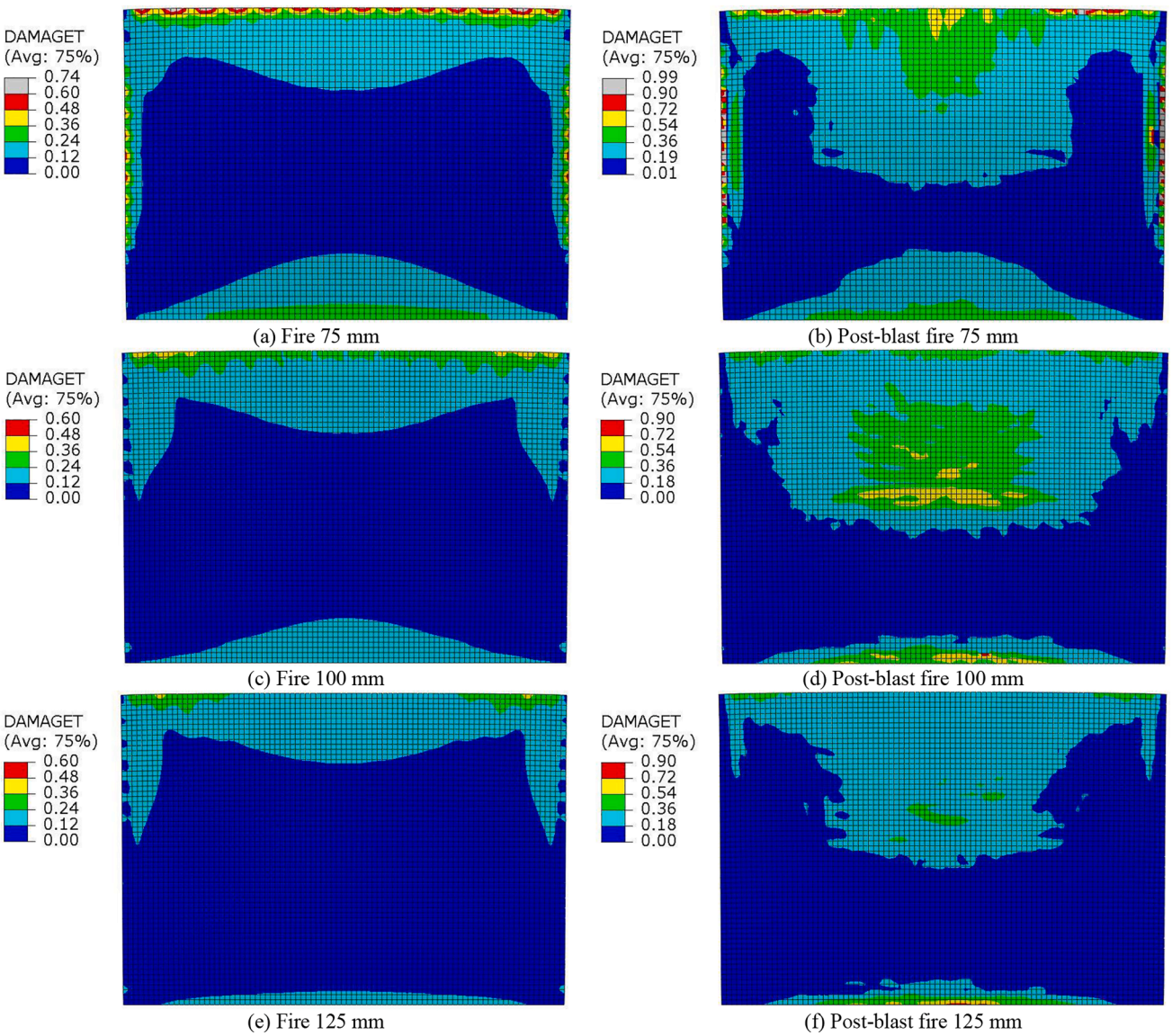

Fig. 13. Tensile damage (d_t) at the unexposed face of the RC wall panels under traditional and post-blast fire.

under the normal fire scenario are obtained as 150 mm, 42.27 mm, and 17.63 mm, respectively, whereas, the maximum responses under the cascaded fire are obtained as 172.70 mm, 72.53 mm, and 10.52 mm, respectively. The fire resistance rating is assessed from the plots using the threshold limit state defined in terms of limiting horizontal out-of-plane deflection in the RC panel under compressive in-plane load to be $h/100 = 43$ mm [41]; where, h represents the height of the member. It is observed that the fire resistance rating of the wall panels with thicknesses 75 mm and 100 mm have decreased significantly from 1.20-h to 1.04-h (13.33%) and from 2-h to 1.55-h (22.5%), respectively. Therefore, these numbers indicate the importance of considering the cascading hazard scenario in the regions where extreme threats are significant to achieve safe and economic design of structures.

Fig. 13 shows tensile damage response (d_t) at the unexposed sides of the RC wall panels under the normal and cascaded fire scenarios. The damage under the cascaded fire scenario is significantly more as compared to the damage caused by normal fire scenario. Mostly, the damage level under the normal fire scenario does not exceed 50% for the RC panels; however, the damage at unexposed face of 75 mm thick wall exceeds 50% and up to 74%, although the exceeded region is observed to be minimal. On the other hand, the tensile damage under the cascading fire at the unexposed face does not exceed 72% mostly; however, the damage in 75 mm thick wall is observed to be exceeding 72% up to 99%, although the exceeded region is observed to be insignificant. The tensile damage due to cascaded fire increases by around 22% at the center, and by around 25% near the edges. Such proportionate increase in damage due to the effect of dynamic blast loading significantly alters the performance of the structures under cascaded fire loading, which requires reconsideration of the design guidelines for structural safety in regions where extreme events, such as accidental blasts occur. Petrochemical industries and alike typically experience such cascading extreme loading events.

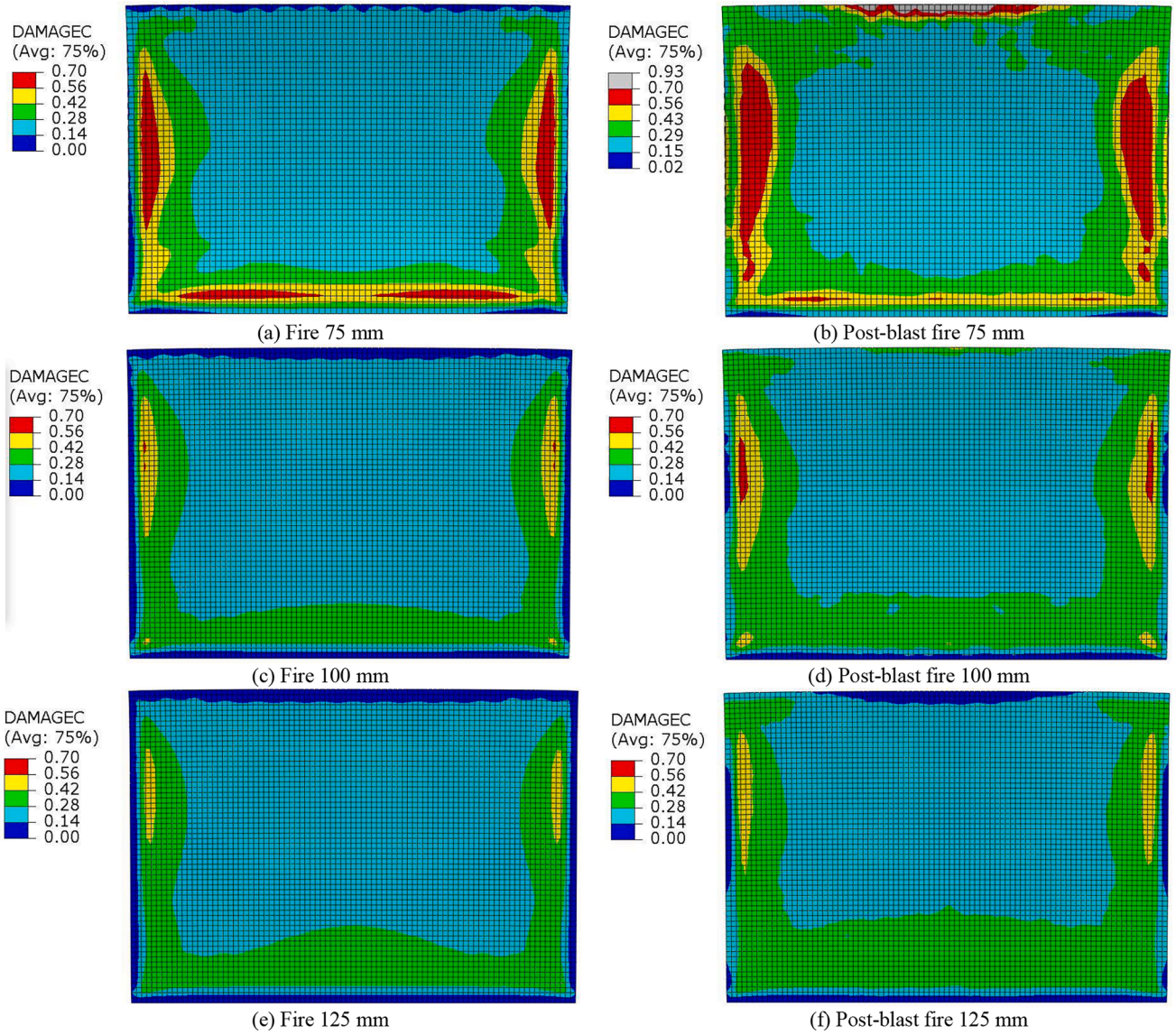

Fig. 14. Compressive damage (d_c) at the exposed face of the RC wall panels under traditional and post-blast fire.

Fig. 14 illustrates the profile of compressive damage (d_c) induced at the exposed face of the RC wall panels under the effects of normal and cascaded fire. The damage levels for the fire scenarios are similar; however, the damaged region under the cascaded fire is significantly higher as compared to the normal fire. Moreover, the compressive damage for the 75 mm thick RC wall panel under the cascaded fire is 93%, which is significantly higher than the damage induced under the normal fire, which is 70%. The excessive damage, i.e., 23% has the tendency to alter the fire resistance rating of the structure, which was clearly observed in Fig. 12. Therefore, there is a desperate need to investigate the performance of structures under the cascaded scenario of post-blast fire considering the pre-damage induced by the extreme blast loading rather than design for individual blast or fire scenarios.

Fig. 15 shows plastic strain profile obtained at the exposed and unexposed faces of the RC wall panels under the normal and cascaded fire. The strains induced at the exposed faces are compressive in nature, whereas the strains induced at the unexposed faces are tensile in nature. As observed, the blast loading induces tensile strains on the exposed and unexposed faces of the RC wall panels. However, on exposure to the fire loading, the exposed face experiences compressive action due to development of compressive strains, while the unexposed face experiences tensile action inducing tensile strains. Therefore, the resultant compressive strains at the exposed face decreases and in comparison with the strains obtained under the normal fire, the peak compressive strains decrease. On the other hand, the resultant tensile strain increases significantly at the unexposed face under the cascaded fire in comparison to the normal fire. The increase in the tensile strain is observed to be in the range from 100% to 170%, which is substantial. With increase in tensile strain, there is relative increase in tensile stress, which is crucial for design of the structural members. The relative increase in the tensile strain will increase the progression of micro-cracking allowing faster rate of propagation of heat to the concrete core, thereby decreasing the fire resistance rating of the structure. Hence, it becomes important to assess the structure under the increased load of cascaded blast and fire to build safe and resilient environment against such extreme events.

Fig. 16 shows plastic equivalent strain ($\varepsilon_{p,eq}$) induced in the RC wall panels under the effect of normal and cascaded fire. The plastic equivalent strain increases substantially under the cascaded fire scenario. The

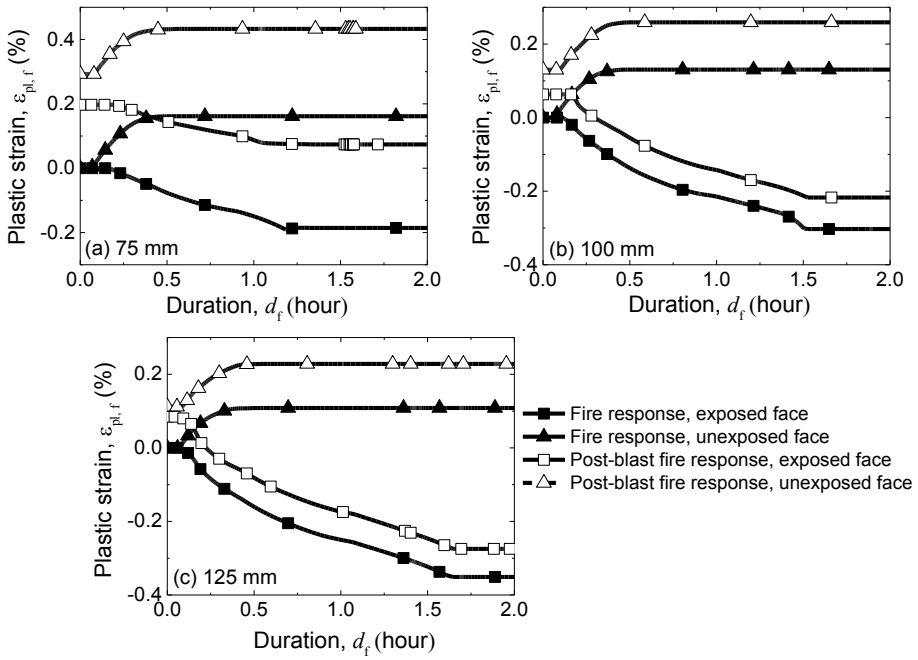

Fig. 15. Evolution of plastic strains at the center of the RC wall panels under traditional and post-blast fire.

equivalent plastic strains for the 75 mm and 100 mm wall panels under the normal fire do not exceed 1% for most of the cases; however, some portion of the exposed face for the 75 mm thick wall exceeds 1% strain and reaching up to 3.6% strain under the cascaded fire scenario. Most of the regions of the exposed faces are induced with 0.4% plastic equivalent strain under the normal fire scenario, whereas the exposed faces under the cascaded fire scenario are induced with 0.6% plastic equivalent strain. There is 50% increase in the plastic equivalent strain under the effect of cascaded fire, which is highly significant considering the design of structures in the regions where extreme threats such as blast is probable. Hence, the increase in the response indicates the importance to consider the effect of cascading hazards for designing new and protecting existing structures. Thus, scenario-based design of the protective structures is essential for ensuring desired level of safety and reliability in their performance under the extreme loading events, such as fire following blast scenario.

8. Conclusions

A novel methodology is presented here to investigate the effects of post-blast fire considering pre-damage induced by blast loading on reinforced concrete (RC) wall panels through finite element (FE) approach. The developed FE model of the RC wall panel is first exposed to blast scenario, and subsequently to an elevated temperature scenario, which involves employing strain-rate models of concrete and steel for dynamic blast analysis and thermal and mechanical properties of concrete and steel for the thermo-mechanical analysis. Responses are compared in terms of deflection, variation of strains, and evolution of damage pattern at the exposed and unexposed faces of the structural member. It is recommended from this investigation to conduct probable scenario-based design of the protective structures. In the context of this investigation, the following conclusions are deduced.

1. The displacement response under the blast loading scenario decreases significantly with proportional increase in thickness of the wall panels. Moreover, for the 125 mm thick RC wall panel, the tensile damage is minimal under the blast loading. Therefore, it is suggested to use wall panel of thickness 125 mm as blast-resistant member for similar range of blast loading scenario.
2. The deflection profiles for wall panels under the cascaded fire effect do not follow the same trend as compared under the normal fire scenario. The fire resistance rating of the wall panels with thicknesses 75 mm and 100 mm have decreased from 1.20-h to 1.04-h (13.33%) and from 2-h to 1.55-h (22.5%), respectively. Therefore, the range of decrease in the fire resistance rating indicate the importance of considering the cascading hazard scenario to guarantee stability of structure and also obtain adequate time to control the fire by rescue teams and safely evacuate the inhabitants in the structure.
3. The damage induced by the cascaded post-blast fire is precisely concentrated around the central region of the wall. The tensile damage due to the post-blast fire increases by around 22% in the central portion, and by around 25% near the edges of the RC wall panel. The increase in damage due to the effect of blast loading significantly alters the performance of the structure under the fire loading, requiring reconsideration of design guidelines for structural safety where such extreme threat scenarios exist.
4. The unexposed face of the RC wall panel experiences an increase in tensile strain from 100% to 170% under the effect of cascading post-blast fire. The substantial increase in the tensile strain proportionately increases the progression of micro-cracking allowing faster rate of propagation of heat to the concrete core, thereby drastically decreasing the fire resistance rating of the structure. Moreover, with such increase in tensile strain, there is relative increase in tensile stress which is crucial for design of any RC members. Hence, it becomes important to assess the structure under the increased load of

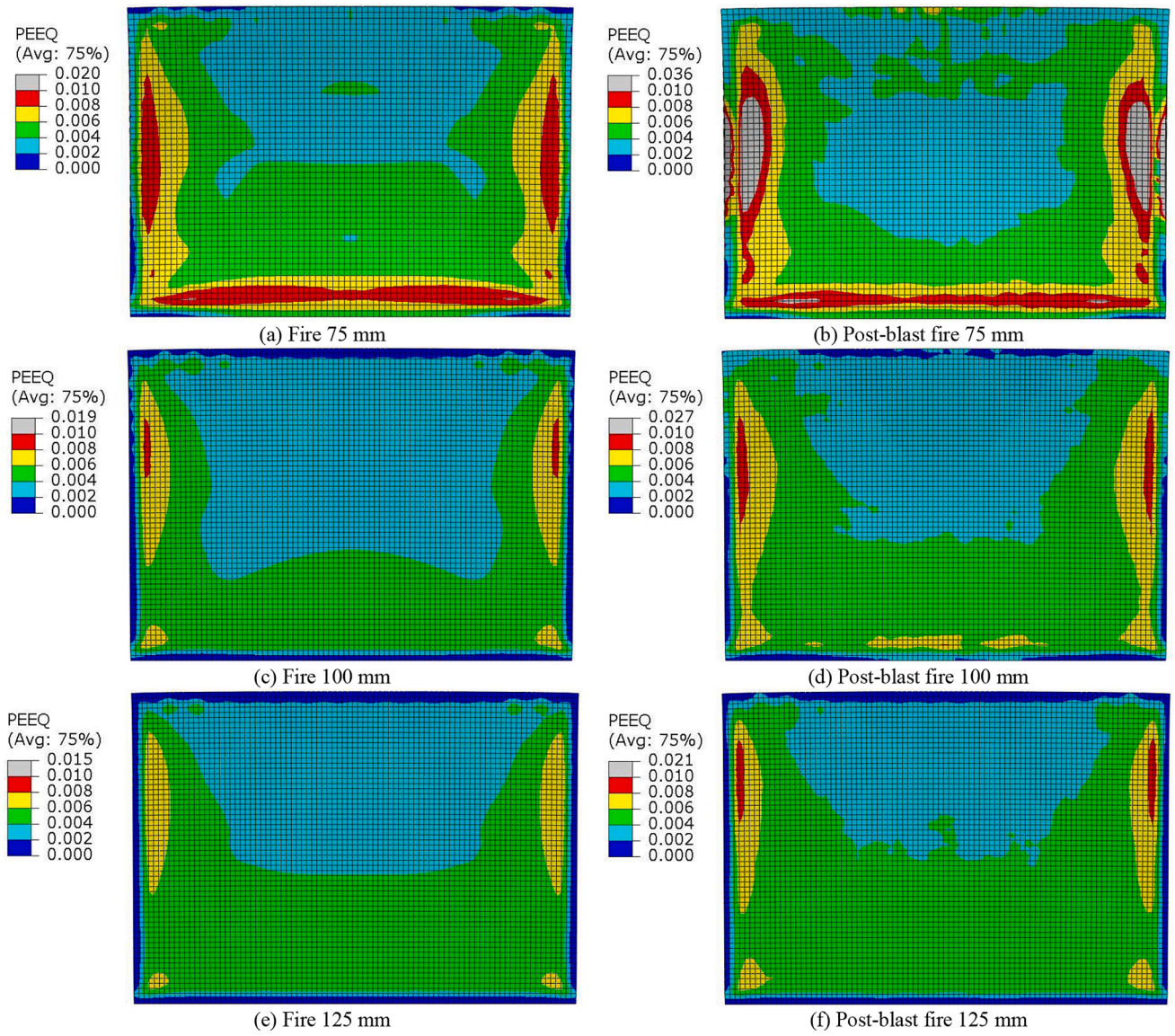

Fig. 16. Plastic equivalent (PEEQ) strains at the exposed face of the RC wall panels under traditional and post-blast fire.

cascaded blast and fire to comprehensively design structural systems against such extreme threats.

Declaration of Competing Interest

The authors declare that they have no known competing financial interests or personal relationships that could have appeared to influence the work reported in this paper.

References

[1] ABAQUS/Standard User's Manual, Version 6.14, Dassault Systemes, Simulia Corporation, Province, Rhode Island (RI), USA.
[2] Alfarah B, López-Almansa F, Oller S. New methodology for calculating damage variables evolution in plastic damage model for RC structures. Eng Struct 2017;132:70–86.
[3] Al-Salloum Y, Almusallam T, Ibrahim SM, Abbas H, Alsayed S. Rate-dependent behavior and modeling of concrete based on SHPB experiments. Cem Concr Compos 2015;55:34–44.
[4] Arablouei A, Kodur V. Modeling delamination of fire insulation from steel structures subjected to blast loading. Eng Struct 2016;116:56–69.
[5] Aslani F, Bastami M. Constitutive relationships for normal-and high-strength concrete at elevated temperatures. ACI Mater J 2011;108(4):355–64.
[6] Asprone D, Cadoni E, Prota A. Experimental analysis on tensile dynamic behavior of existing concrete under high strain rates. ACI Struct J 2009;106(1):106–13.
[7] Baker WE. Explosions in air, University of Texas Press, Austin, Texas (TX), USA; 1973.
[8] Behnam B, Ronagh H. An engineering solution to improve post-earthquake fire resistance in important reinforced concrete structures. Adv Struct Eng 2014;17(7):993–1009.
[9] Bhatt P, Kodur V, Matsagar V. Numerical approach to evaluate elevated temperature behavior of steel fiber reinforced concrete columns. Indian Concr J 2019;93(8):8–15.
[10] Binder E, Wang H, Zhang J-L, Schlappal T, Yuan Y, Mang HA, et al. Application-oriented fundamental research on concrete and reinforced concrete structures: selected findings from an Austro-Chinese research project. Acta Mech 2020;231(6):2231–55. https://doi.org/10.1007/s00707-020-02639-1.
[11] Chang YF, Chen YH, Sheu MS, Yao GC. Residual stress-strain relationship for concrete after exposure to high temperatures. Cem Concr Res 2006;36(10):1999–2005.
[12] Chaudhary RK, Roy T, Matsagar V. Framework for fragility assessment of reinforced concrete portal frame subjected to elevated temperature. Structures 2020;28:2785–800.
[13] Chaudhary RK, Roy T, Matsagar V. Member and structural fragility of reinforced concrete structure under fire. J Struct Fire Eng 2020;11(4):409–35.
[14] Chen Li, Fang Q, Jiang X, Ruan Z, Hong J. Combined effects of high temperature and high strain rate on normal weight concrete. Int J Impact Eng 2015;86:40–56.
[15] Choubey B, Dutta SC, Prakhya GKV, Mandal P, Kumar Tanwar R. Blast pressure analysis due to confined explosion-after effects. Structures 2020;28:521–36.
[16] Colombo M, Martinelli P, di Prisco M. A design approach for tunnels exposed to blast and fire. Struct Concr 2015;16(2):262–72.
[17] Comite Euro-International du Beton (1993), CEB-FIP Model Code (1990) Design Code. Thomas Telford Services Ltd., Lausanne, London, UK; 1990.

[18] Conley C, Williamson EB, Thiagarajan G. "Behavior of concrete structures subjected to blast and impact", American Concrete Institute (ACI) Fall 2010 Convention, SP-281, Pittsburgh, Pennsylvania (PA), USA; 2010.
[19] Corley WG. Lessons learned on improving resistance of buildings to terrorist attacks. J Perform Constr Facil (ASCE) 2004;18(2):68–78.
[20] Corley WG, Sr. PFM, Sozen MA, Thornton CH. The Oklahoma City bombing: summary and recommendations for multi-hazard mitigation. J Perform Constr Facil (ASCE) 1998;12(3):100–12.
[21] Cui J, Hao H, Shi Y. Discussion on the suitability of concrete constitutive models for high-rate response predictions of RC structures. Int J Impact Eng 2017;106: 202–16.
[22] EC1. Eurocode 1: actions on structures – Part 1–2: general actions – actions on structures exposed to fire. European Committee for Standardization, Brussels, Belgium; 2002.
[23] EC2 Part 1-2. Eurocode 2: design of concrete structures – Part 1-2: general rules – structural fire design, European Committee for Standardization, Brussels, Belgium; 2004.
[24] Fujikura S, Bruneau M. Dynamic analysis of multi-hazard-resistant bridge piers having concrete-filled steel tube under blast loading. J Bridge Eng (ASCE) 2012;17 (2):249–58.
[25] Gardner L, Bu Y, Francis P, Baddoo NR, Cashell KA, McCann F. Elevated temperature material properties of stainless-steel reinforcing bar. Constr Build Mater 2016;114:977–97.
[26] Goel MD, Matsagar VA. Blast-resistant design of structures. Pract Period Struct Design Constr (ASCE) 2014;19(2):04014007. https://doi.org/10.1061/(ASCE) SC.1943-5576.0000188.
[27] Goel MD, Matsagar VA, Gupta AK, Marburg S. An abridged review of blast wave parameters. Defence Sci J 62 (5): 2012; 300–306. https://doi.org/10.14429/ dsj.62.1149.
[28] Hao H, Hao Y, Li J, Chen W. Review of the current practices in blast-resistant analysis and design of concrete structures. Adv Struct Eng 2016;19(8):1193–223.
[29] Heidari M, Robert F, Lange D, Rein G. Probabilistic study of the resistance of a simply-supported reinforced concrete slab according to Eurocode parametric fire. Fire Technol 2019;55(4):1377–404.
[30] Hetherington J, Smith P. Blast and ballistic loading of structures. Oxford, UK: Butterworth-Heinemann; 1994.
[31] IS 456. Plain and reinforced concrete – code of practice. Bureau of Indian Standards (BIS), New Delhi, India; 2000.
[32] ISO 834. Fire resistance tests – elements of building construction. International Organization for Standardization, Geneva, Switzerland; 1999.
[33] Jain S, Tiwari R, Chakraborty T, Matsagar VA. Dynamic response of reinforced concrete wall under blast loading. Indian Concr J 2015;89(8):27–41.
[34] Jin L, Bai J, Zhang R, Li L, Du X. Effect of elevated temperature on the low-velocity impact performances of reinforced concrete slabs. Int J Impact Eng 2021;149: 103797. https://doi.org/10.1016/j.ijimpeng.2020.103797.
[35] Jin L, Zhang R, Dou G, Du X. Fire resistance of steel fiber reinforced concrete beams after low-velocity impact loading. Fire Saf J 2018;98:24–37.
[36] Kakogiannis D, Pascualena F, Reymen B, Pyl L, Ndambi JM, Segers E, Lecompte D, Vantomme J, Krauthammer T. Blast performance of reinforced concrete hollow core slabs in combination with fire: numerical and experimental assessment. Fire Saf J 2013;57:69–82.
[37] Khan S, Saha SK, Matsagar VA, Hoffmeister B. Fragility of steel frame buildings under blast load. J Perform Constr Facil (ASCE) 2017;31(4):04017019. https://doi. org/10.1061/(ASCE)CF.1943-5509.0001016.
[38] Kinney GF, Graham KJ. Explosive shocks in air. 2nd Ed., Springer, Berlin, Germany; 1985.
[39] Kodur V. Properties of concrete at elevated temperatures. ISRN Civil Eng 2014; 2014:1–15.
[40] Kodur VKR, Sultan MA. Effect of temperature on thermal properties of high-strength concrete. J Mater Civ Eng 2003;15(2):101–7.
[41] Kumar P, Kodur VKR. Modeling the behavior of load bearing concrete walls under fire exposure. Constr Build Mater 2017;154:993–1003.
[42] Lam N, Mendis P, Ngo T. Response spectrum solutions for blast loading. Electron J Struct Eng 2004;4:28–44.
[43] Lee J, Fenves GL. Plastic-damage model for cyclic loading of concrete structures. J Eng Mech (ASCE) 1998;124(8):892–900.
[44] Lee J, Fenves GL. A plastic-damage concrete model for earthquake analysis of dams. Earthq Eng Struct Dyn 1998;27(9):937–56.
[45] Lee J, Fenves GL. A return-mapping algorithm for plastic-damage models: 3-D and plane stress formulation. Int J Numer Meth Eng 2001;50(2):487–506.
[46] Liew JYR, Chen H. Explosion and fire analysis of steel frames using fiber element approach. J Struct Eng (ASCE) 2004;130(7):991–1000.
[47] Lu D, Wang G, Du X, Wang Y. A nonlinear dynamic uniaxial strength criterion that considers the ultimate dynamic strength of concrete. Int J Impact Eng 2017;103: 124–37.
[48] Lubliner J, Oliver J, Oller S, Oñate E. A plastic-damage model for concrete. Int J Solids Struct 1989;25(3):299–326.
[49] Luccioni BM, Ambrosini RD, Danesi RF. Analysis of building collapse under blast loads. Eng Struct 2004;26(1):63–71.
[50] Matsagar VA. Materials for sacrificial blast wall as protective structure. Proc Indian Natl Sci Acad (INSA) 2013;79(4):717–23. https://doi.org/10.16943/ptinsa/2013/ v79i4/48006.
[51] Matsagar VA. Computing stress and displacement response of composite plates under blast. Disaster Adv 2014;7(1):23–8.
[52] Matsagar VA. Comparative performance of composite sandwich panels and non-composite panels under blast loading. Mater Struct 2016;49:611–29. https://doi. org/10.1617/s11527-015-0523-8.
[53] Matsagar VA. Multi-hazard protective structures for blast and fire. 63rd International congress of the Indian society of theoretical and applied mechanics (ISTAM), Bangalore, India; 2018. https://istam.iitkgp.ac.in/resources/2018/ proceedings/speakers/IL_vasant.pdf.
[54] Mirmomeni M, Heidarpour A, Zhao X-L, Packer JA. Effect of elevated temperature on the mechanical properties of high-strain-rate-induced partially damaged concrete and CFSTs. Int J Impact Eng 2017;110:346–58.
[55] Ngo T, Fragomeni S, Mendis P, Ta B. Testing of normal-and high-strength concrete walls subjected to both standard and hydrocarbon fires. ACI Struct J 2013;110(3): 503–10.
[56] Noguchi T, Tomosawa F, Nemati KM, Chiaia BM, Fantilli AR. A practical equation for elastic modulus of concrete. ACI Struct J 2009;106(5):690–6.
[57] Prochazka Petr P. Effect of explosion and fire on underground structures. Int J Protect Struct 2013;4(4):505–20.
[58] Rezvani FH, Behnam B, Ronagh HR, Jeffers AE. Robustness assessment of a generic steel fire-protected moment-resisting frame under travelling fire. Eur J Environ Civil Eng 2018;22(1):64–81.
[59] Roy T, Matsagar V. Fire fragility of reinforced concrete panels under transverse out-of-plane and compressive in-plane loads. Fire Saf J 2020;113:102976. https:// doi.org/10.1016/j.firesaf.2020.102976.
[60] Ruan Z, Chen L, Fang Q. Numerical investigation into dynamic responses of RC columns subjected for fire and blast. J Loss Prev Process Ind 2015;34:10–21.
[61] Schleyer GK, Campbell D. Development of simplified analytical methods for predicting the response of offshore structures to blast and fire loading. Mar Struct 1996;9(10):949–70.
[62] Silva PF, Lu B. Blast resistance capacity of reinforced concrete slabs. J Struct Eng (ASCE) 2009;135(6):708–16.
[63] Song L, Izzuddin BA, Elnashai AS, Dowling PJ. An integrated adaptive environment for fire and explosion analysis of steel frames – part I: analytical models. J Constr Steel Res 2000;53(1):63–85.
[64] Soroushian P, Choi K. Steel mechanical properties at different strain rates. J Struct Eng (ASCE) 1987;113(4):663–72.
[65] Sozen MA, Thornton CH, Corley WG, Mlakar PF. The Oklahoma City bombing: structure and mechanisms of the Murrah building. J Perform Constr Facil (ASCE) 1998;12(3):120–36.
[66] UFC 3-340-02. Structures to resist the effects of accidental explosions. US Department of Defense, Washington – District of Columbia (DC), USA; 2008.
[67] Vitorino H, Rodrigues H, Couto C. Evaluation of post-earthquake fire capacity of a reinforced concrete one bay plane frame under ISO fire exposure. Structures 2020; 23:602–11.
[68] Wang J, Chen W, Guo Z, Liang W. Dynamic responses of RPC-filled steel tubular columns post fire under blast loading. Open Civil Eng J 2016;10(1):236–45.
[69] Yu HX, Liew JYR. Steel framed structures subjected to the combined effects of blast and fire - part 1: state-of-the-art review. Adv Steel Constr 2005;1(1):79–96.
[70] Yu X, Chen L, Fang Q, Ruan Z, Hong J, Xiang H. A concrete constitutive model considering coupled effects of high temperature and high strain rate. Int J Impact Eng 2017;101:66–77.
[71] Zhai C, Chen L, Xiang H, Fang Q. Experimental and numerical investigation into RC beams subjected to blast after exposure to fire. Int J Impact Eng 2016;97:29–45.
[72] Zhao J, Fang Q, Chen L, Li D. Numerical analysis of fire resistance of RC beams subjected to explosion and fire load. J Tianjin Univ Sci Technol 2015;48(10): 873–80.
[73] Zhou XQ, Hao H. Modelling of compressive behavior of concrete-like materials at high strain rate. Int J Solids Struct 2008;45(17):4648–61.